AUTHOR QUERY FORM

ELSEVIER	**Book: Dodd1630104** **Chapter: CH003**	**Please e-mail your responses and any corrections to:** **E-mail: s.sambandam@elsevier.com**

Dear Author,

Any queries or remarks that have arisen during the processing of your manuscript are listed below and are highlighted by flags in the proof. (AU indicates author queries; ED indicates editor queries; and TS/TY indicates typesetter queries.) Please check your proof carefully and answer all AU queries. Mark all corrections and query answers at the appropriate place in the proof (e.g., by using on-screen annotation in the PDF file http://www.elsevier.com/framework_authors/tutorials/ePDF_voice_skin.swf) or compile them in a separate list, and tick off below to indicate that you have answered the query.
Please return your input as instructed by the project manager.

Uncited references: References that occur in the reference list but are not cited in the text. Please position each reference in the text or delete it from the reference list.	
Missing references: References listed below were noted in the text but are missing from the reference list. Please make the reference list complete or remove the references from the text.	

Location in Article	Query / remark	
AU:1, Page 111	Please confirm whether the edit made to the title is OK.	
AU:2, Page 111	Please confirm whether the affiliations are OK as given.	
AU:3, Page 171	Please confirm whether the edit made to the sentence "Thus, a band ... etching characteristics." is OK.	
AU:4, Page 111	Please note that the entries "θ^*," "ρ," and "D" have been given twice in the nomenclature. Therefore, we have deleted the latter entries. Please confirm whether this is OK.	
AU:5, Page 113	Please spell out TEM, if necessary.	
AU:6, Page 113	Please note that "TREM" given here and elsewhere in this chapter has been changed as "HREM."	
AU:7, Page 113	Please spell out HREM, if necessary.	
AU:8, Page 113	Please note that "FEGSEM" has been changed as "FESEM" here and elsewhere in this chapter.	
AU:9, Page 115	Please spell out SHTB, if necessary.	
AU:10, Page 118	Please note that "thermal conductility" given here has been changed as "thermal conductivity."	
AU:11, Page 118	Please note that the references have been renumbered to make them sequential with the text.	

AU:12, Page 120	Please confirm whether the unit "K/s" given here is OK.	
AU:13, Page 121	Please add the closing quote mark (') for this beginning quote.	
AU:14, Page 122	Please note that "con-focus laser scanning microscopy" has been changed as "confocal laser scanning microscopy" and its abbreviation has been changed as CLSM through-out this chapter. Please confirm whether this is OK.	
AU:15, Page 128	Please confirm whether the insertion of "Chapter 7" in the sentence "In Chapter 7 ... granular materials." is OK.	
AU:16, Page 129	Since this is a monocolor job, please rephrase the sen-tences which describe colors.	
AU:17, Page 130	Please spell out TWIP, if necessary.	
AU:18, Page 132	Please spell out ND, if necessary.	
AU:19, Page 140	Are you referring to Section 7.2 in Chapter 7 or should this be Section 3.2 for this chapter?	
AU:20, Page 142	Please spell out DRX, if necessary.	
AU:21, Page 143	Please spell out FCC, if necessary.	
AU:22, Page 145	Please spell out SADP, if necessary.	
AU:23, Page 146	Please confirm whether the sentence "Figure 3.35A is ... respectively." is OK as edited.	
AU:24, Page 156	Please spell out UFG, if necessary.	
AU:25, Page 157	Please confirm whether the insertion of expansion of ECAP is OK.	
AU:26, Page 163	The sense of the sentence "Deformation at ... of a second." seems to be unclear. Please rephrase the sentence for better clarity.	
AU:27, Page 163	Please suggest whether "GESEM" should be changed as "FESEM."	
AU:28, Page 170	Please note that ref. 119 (originally numbered) was not cited anywhere in the text. Therefore, the references have been renumbered and the uncited reference (new no. 163) is kept at the end of the list. Kindly cite it in the text or delete it from the reference list.	
AU:29, Page 164	Please provide the chapter title for ref. 10.	
AU:30, Page 165	Please provide the article title for refs. 11 and 12.	
AU:31, Page 165	Please provide the location of the publisher for refs. 17 and 18.	

AU:32, Page 165	Please provide the article title for ref. 32.	
AU:33, Page 165	Please provide the location of the publisher for ref. 35.	
AU:34, Page 166	Please provide the article title for refs. 38−44.	
AU:35, Page 166	Please provide the chapter title for ref. 47.	
AU:36, Page 166	Please confirm whether the title of ref. 48 is OK as given.	
AU:37, Page 166	Please provide the chapter title for ref. 58.	
AU:38, Page 166	Please provide the location of the publisher for ref. 59.	
AU:39, Page 167	Please provide the article title for ref. 64.	
AU:40, Page 167	Please provide the article title for ref. 67.	
AU:41, Page 167	Please provide the article title for ref. 74.	
AU:42, Page 167	Please provide the article title for ref. 78.	
AU:43, Page 167	Please provide the editor names and location of the publisher for ref. 82.	
AU:44, Page 168	Please provide the article title for refs. 83 and 84.	
AU:45, Page 168	Please provide the article title for refs. 91 and 92.	
AU:46, Page 168	Please provide the article title for refs. 96−100.	
AU:47, Page 168	Please provide the article title for refs. 102 and 103.	
AU:48, Page 168	Please provide the article title for ref. 107.	
AU:49, Page 169	Please provide the chapter title for ref. 109.	
AU:50, Page 169	Please provide the article title for ref. 118.	
AU:51, Page 169	Please provide the article title for refs. 120 and 121.	
AU:52, Page 169	Please provide the chapter title for ref. 122.	
AU:53, Page 169	Please provide the article title for ref. 124.	
AU:54, Page 169	Please provide the location of the publisher for ref. 126.	
AU:55, Page 169	Please provide the article title for refs. 127−136.	
AU:56, Page 170	Please provide the article title for ref. 138.	
AU:57, Page 170	Please provide the article title for ref. 141.	
AU:58, Page 170	Please provide the article title for ref. 143.	

AU:59, Page 170	Please provide the article title for refs. 147−150.	
AU:60, Page 170	Please provide the article title for refs. 152 and 153.	
AU:61, Page 170	Please provide the article title for refs. 156−162.	
AU:62, Page 124	Please note that "εef" given here has been changed as "εeff."	
AU:63, Page 146	Please confirm whether the edit made to the legend of Figure 3.33 is OK.	
AU:64, Page 114	There is a discrepancy in the caption of Table 1 given in the chapter and in the table.doc. Please confirm whether the table caption given here is appropriate. Also check whether the table is OK as edited.	
AU:65, Page 111	Please spell out the first name of the authors, if necessary.	
AU:66, Page 138	Please confirm whether the edit made to the sentence "Rath and Hu. . ."grain-boundary purity.	

c0003 # 3 Nanostructural and Microstructural Aspects of Shear Localization at High-Strain Rates for Materials

AU : 1

Y.B. Xu[1] and M.A. Meyers[2,3]

AU : 65

[1]Shenyang National Laboratory for Materials Science, Institute of Metal Research, Chinese Academy of Sciences, Shenyang, People's Republic of China, [2]Department of Mechanical and Aerospace Engineering, University of California, San Diego, CA, [3]Department of Nanoengineering, University of California, San Diego, CA

AU : 2

Nomenclature[1]

AU : 4

α' martensite phase
σ_f fracture strength
n work-hardening exponent
γ strain
$\dot{\gamma}$ strain rate
γ_c average critical strain
δ half-width of the shear band
θ_* the temperature rise in the band
$\vec{F}$ force acting on a particle (a mechanical stress induces diffusion)
∇V the gradient of the potential energy field
$\vec{v}$ the mean diffusion velocity
J the flux along a grain boundary with thickness δ and depth L_2 (cross-sectional area $L_2\delta$)
D the diffusion coefficient
C the concentration of the mobile species (expressed in terms of mass per unit volume)
θ the grain-boundary rotation angle
dV the volume transferred
L the instantaneous length of the segment of the grain boundary in the rotational recrystallization model
L_1 the initial length of the grain boundary in the rotational recrystallization model
ρ material density
δD_{GB} the grain-boundary diffusion coefficient
M the grain-boundary mobility (the proportionality constant)
d the grain size
D_2 the average diameter of the recrystallized grains

[1] Other symbols used are defined in the text.

γ_c the critical strain stopping the subgrain rotation
η the boundary energy density
D the equivalent diameter of the cell structure (or subgrain)
D_B^V vacancy diffusion coefficient
D_{B_0} the grain-boundary diffusion coefficient
Q_B the activation energy of the grain-boundary diffusion
λ the coefficient of the heat conduction
c the heat capacity
$\dot{\varepsilon}$ the minimum strain rate occurring in serrated flow
Q the activation energy for diffusion
C the frequency factor

3.1 Introduction
s0010

p0205 The occurrence of localized shear bands, as an inevitable outcome of thermoplastic instability induced under high strain and high-strain rate, has been a topic of great interest to scientists and engineers, and thus a great deal of investigation has been made experimentally and theoretically since its first recognition made by Zener and Hollomon [1]. Indeed, there was an earlier observation by Tresca in the nineteenth century, during deformation of platinum. Because of its scientific and technological importance, it poses an interesting challenge to researchers, and much attention has been received during the past several decades. The number of contributions on this topic is of the order of 1,200, and there has been a monotonic increase from the 1980s to 2007, with a plateau being reached of ~ 200 papers per year. This is a substantial and global effort. This chapter, with less than 200 references, is not comprehensive and emphasizes our own work, with mention of other contributions. This should not be understood as an effort to ignore the important literature but a necessity of space limitation.

p0210   Mechanicians have focused their efforts on the macro-description of the constitutive models, developing the criteria required for the onset and propagation of thermal plastic instability [2−12]. Most of these approaches consist of a combination of mechanical and thermal instability analysis. On the other hand, however, material scientists have focused on the microstructural and nanostructural aspects of localized shear deformation, concerning the effects of the materials and structures on the formation of shear localization. There are a number of extensive reviews [13−19] and special articles [20−34] published on the microstructural aspects of shear banding.

p0215   In this chapter, we will focus on the observation and analysis of the shear localization evolution and microstructures in metals and alloys, although, in various conditions, other materials such as some polymers, granular media and metallic glasses are sensitive to adiabatic shearing. We focus here on imposed strain-rate regimes of 10^{-3} to $10^6 \, \mathrm{s}^{-1}$ at ambient temperature and on results of research carried out over the past 20 years. The emphasis is placed on the mechanical conditions required for the shear localization and microstructural evolution induced by

dynamic torsional, impact compression, as well as the explosive collapse of thick-walled cylinders (TWCs).

s0015 3.2 Modern Techniques for Microstructural Characterization

p0220 The physical, chemical and, in particular, mechanical behaviour of metallic and non-metallic materials are sensitive to the microstructure and nanostructure. In other words, these properties of the materials are closely connected to their structures, including morphology, crystal structure and chemical composition on the micro scale. Scientists and engineers have been sparing no effort to manufacture and improve research tools for the characterization of microstructures of the materials accompanying the advance of science and technology. In the long history of the development of characterization instruments, perhaps the greatest impact is the emergence of TEM, which has become one of the primary tools for characterizing the nano-, micro- and meso-structures of materials because of its high-resolution capabilities. For example, the commercial TEM is now routinely available with point resolution better than 2 Å (0.2 nm), and the HREM is now capable of producing interpretable information approaching 1 Å provided the sample examined is sufficiently thin [35]. The development of TEM as a magnifying tool has taken place since the end of 1940s. Since the 1950s, bright-field, dark-field and diffraction contrast analyses have been extensively applied to structural analysis, leading to an in-depth understanding of the structure of materials, especially direct observation of the crystal defects such as dislocations and stacking faults in thin crystals [36]. In addition to these, small-angle diffraction, high-resolution diffraction, as well as convergent beam electron diffraction and other techniques can also be chosen for various purposes. However, the narrow region of the shear bands (of the order of one to several micrometres) renders the microscopic examination difficult. In spite of its high resolution, TEM still appears to have limitations for investigating the microstructures of the bands because the perforation produced using the common electropolishing method does not usually coincide with the band area. On the other hand, the choice of the field observed on the specimen is significantly restricted. Therefore, improper and even mistaken information introduced from the thin foil is inevitable sometimes, leading to confusion in interpreting images. Electron probe microanalysis (EPMA), developed based on the TEM in 1960s, has been applied rapidly to the micro-area of chemical composition determination approaching 1 μm. Scanning electron microscopy (SEM), based on the EPMA, appeared in 1965. It has revolutionized material-related fractographic studies where comparisons of fracture surfaces may be made with archival results to identify sources of failure and consequent failure mechanisms. A recent great headway is the coupling of SEM with electron backscatter diffraction (EBSD), particularly the use of EBSD in conjunction with a field-emission SEM (FESEM). EBSD is a relatively new technique and has been widely employed to characterize subgrain structures recently. The advantages of EBSD related to optical microscopy as the quantitative metallographic method are higher spatial resolution, more accurate

AU : 5

AU : 6
AU : 7

AU : 8

Table 3.1 Electron-Based Techniques and Their Application
in Microstructure/Nanostructure Characterization

Information	Imaging	Diffraction, Contrast Effects	Micro-Chemical	Analyzers
Trans.-E	TEM	HEED, Kikuchi	—	TEM
	STEM	HEED, Kikuchi	—	TEM, SEM
CELE	ECTEM	—	CELS	TEM
BSE	SEM	ECP, EBSD	BSC-Z	EPMA, SEM
SE	SEM	ECP	—	EPMA, SEM
AE	SEM	ECP	AEC-Z	EPMA, SEM
Auger-E	SEM	—	AES	AES, SEM
LEE	—	LED	—	LEDS
C-Ray	XRMS	Kossel	CXES	EPMA, SEM, TEM

Trans.-E, transmission electron; CELE, characteristic energy lost electron; BSE, backscatter electron; SE, secondary electron; AE, absorbed electron; Auger-E, Auger electron; LEE, low energy electron; C-Ray, characteristic X-ray.

data and more complete structure characterization. In particular, EBSD in an FESEM can reduce the angular resolution to $\sim 0.01°$ and allows quantitative analysis of grain and subgrain size as small as $\sim 0.2\,\mu m$. Humphreys [37] has compared and summarized the advantages and disadvantages of EBSD relative to other metallographic techniques. The advantages of EBSD over the TEM are as follows:

u0010 • The microstructural analysis can be made of the bulk materials rather than thin foils, avoiding the production of improper and even mistaken information arising from the observation.

u0015 • Information is accurately and easily obtained from a specific area of interest, which is important and powerful for the narrow size of shear bands.

u0020 • Rapid and automated acquisition and analysis of diffraction patterns, which is not routinely available in the TEM, enables many thousands of grain/subgrains to be characterized from a single map.

p0240 The disadvantages of EBSD relative to TEM might include the following:

u0025 • Worse spatial resolution cannot image individual dislocations, nanometre-sized grains and defects.

u0030 • Longer time is required for data acquisition.

p0255 Techniques arising from the modern instruments for microstructure/nanostructure characterization are summarized in Table 3.1.

s0020 ## 3.3 The Process of Shear Localization Evolution

p0260 The evolution of shear localization has stimulated a considerable number of theoretical and experimental investigations. Among the analytical approaches, the following are noteworthy:

u0035 • Criteria proposed by Zener and Hollomon [1], Recht [2] and Culver [3] are exclusively based on the effects of work hardening, thermal softening and strain-rate sensitivity.

u0040 • Perturbation analyses of Molinari and Clifton [38], Bai [4] and Grady and Kipp [39] represent a significant advance over the simpler first-generation analyses.

u0045 • Finite element formulation in various forms (e.g. Kuriyama and Meyers [40]).

u0050 • Spacing of shear bands, which was theoretically treated by Grady and Kipp [39], Wright and Ockendon [41] and Molinari [42].

p0285   Additional noteworthy studies are by Clifton et al. [43], Bai et al. [44], Shawki and Clifton [45] and Liao and Duffy [46]. A number of scaling laws have been obtained by Backman et al. [47], Bai [48] and Dodd et al. [49]. However, the analysis of localized plastic shear deformation is still limited by a lack of critical comparisons of theory and experiment. Some experimental attempts to measure the process of shear localization have been made. Costin et al. [50] are known to have made the first measurement of the temperature history of shear localization, and later Hartley et al. [51] have improved their infrared technique and measured the temperature distribution. They assumed that the localized shear process was divided into three consecutive stages. In the first stage, the grid lines incline but remain straight, implying that the deformation is homogeneous. In the second stage, the grid lines become slightly curved, indicating inhomogeneous deformation. In the third stage, the grid lines appear discontinuous, implying shear-band formation. Marchand and Duffy [21] and Giovanola [52] have independently observed the transient deformation field of the shear process by high-speed photography and a grid pattern. More recently, Guduru et al. [53] obtained detailed in situ temperature profiles at the shear-band tips in a C-300 Maraging steel. They focused on the tips of the band using a 2D infrared radiation (IR) array with an acquisition rate of 10^6 frames per second. They observed that the front contained 'hot spots' with a spacing of ~ 0.25 to 1 mm, which they attributed to velocity effects. They report local temperature rises of up to 600 K.

p0290   All of these works certainly have blazed a trail in the experimental study of the localized process, but they have not revealed the evolution process in microstructure occurring during shearing and have not clarified the relationship of the mechanical parameters with the microstructures in the band. The main reason for this is that the original SHTB could not be used to study the microstructure evolution occurring during localization. Bai, Xue and co-workers [25,54,55] modified the original SHTB, which enabled them to combine ingeniously the measurements of the mechanical parameters (stress and strain) at successive points on the $\tau - \gamma$ curve with correlated microstructural observation and to follow the formation and evolution processes of the bands. Figure 3.1 shows four interrupted tests on the four stress−strain curves with four prescribed loading durations labelled a, b, c and d for Ti−6Al−4V alloys subjected to torsional loading at an average strain rate of $3.1 \times 10^3 \, s^{-1}$ [25]. The curves overlap, the difference being the maximum strain that each specimen undergoes. There is a node in the curve at which the average critical strain is 0.160. The specimen with terminal point a is loaded for 450 μs, showing a maximum strain of 0.160, and it represents the state near the critical point. There is no kink on the curve, implying the specimen is still in homogeneous deformation, and no microstructural change is observed during this regime of homogeneity. Beyond this point, the stress drops slowly. The specimen with terminal point b, loaded for 550 μs, attained a nominal strain of 0.196 before unloading.

AU : 9
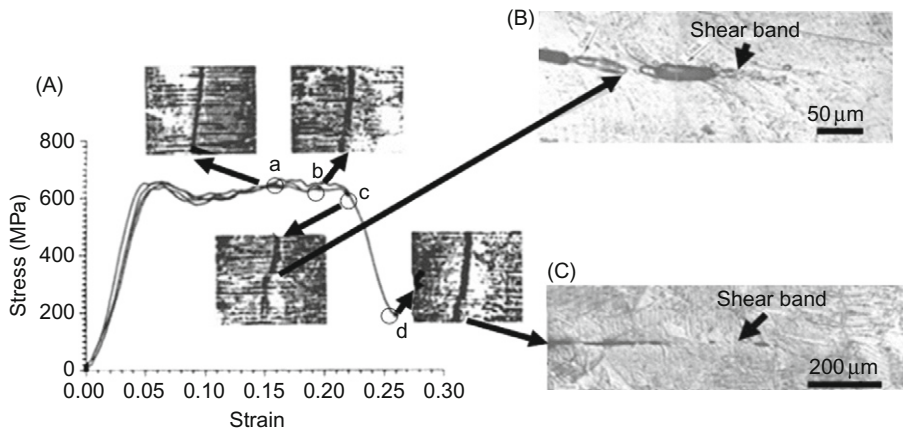
f0010   **Figure 3.1** Stress−strain response of Ti−6Al−4 V alloys subjected to dynamic torsional loading and the corresponding patterns of the inside scribe lines [25].

Local maxima and minima in the stress−strain curve for this sample is suggestive of inhomogeneous deformation. Observation displays the distinct occurrence of shear localization; the width of the shear zone is about 44 μm, and maximum shear strain is 1.07, which is five times the average value. A tiny elliptical void can be seen within the shear zone (Figure 3.1B). More interesting is that the width of the local shear zone is much narrower than the size of the grain, but its extension covers several grains. Loaded for 650 μs, a specimen with terminal point c gained a nominal strain of 0.219. Severe localized shear bands appeared. Obviously, the micro-voids have grown, and some of them have coalesced into a large crack (Figure 3.1C). They even extend from one grain to another. There are still some uncracked segments in the band. Near the crack tip, the band is 20 μm wide, attaining a strain of 0.214. The occurrence of the band does not significantly affect the capacity of the material for continued deformation (point c). In fact, the steep drop in the shear stress appears only after point c. A specimen with terminal point d is subjected to a larger average strain of 0.26 but much lower stress, only one-third of that at the critical point. A long crack has formed along the band (Figure 3.1C). The half-width of the band is about 10 μm. Typically, the sudden drop in the $\tau-\gamma$ curve has been described as a catastrophic failure due to the localized shearing. These observations of both stress−strain response behaviour and related microstructure suggest that the critical mechanism governing the loss in load-carrying capacity is the coalescence of the micro-cracks (voids) within the band, rather than shear-band formation. Similarly, Figure 3.2 shows the localized process of shear deformation in Al−Li alloy subjected to dynamic torsion with an average strain rate of about $2.3 \times 10^3 \, s^{-1}$ [56]. It was found that when the average strain is ∼0.10, corresponding to a loading time of 40 μs, the deformation appears to be homogeneous (Figure 3.2A), and there is no shear localization to be recognized on
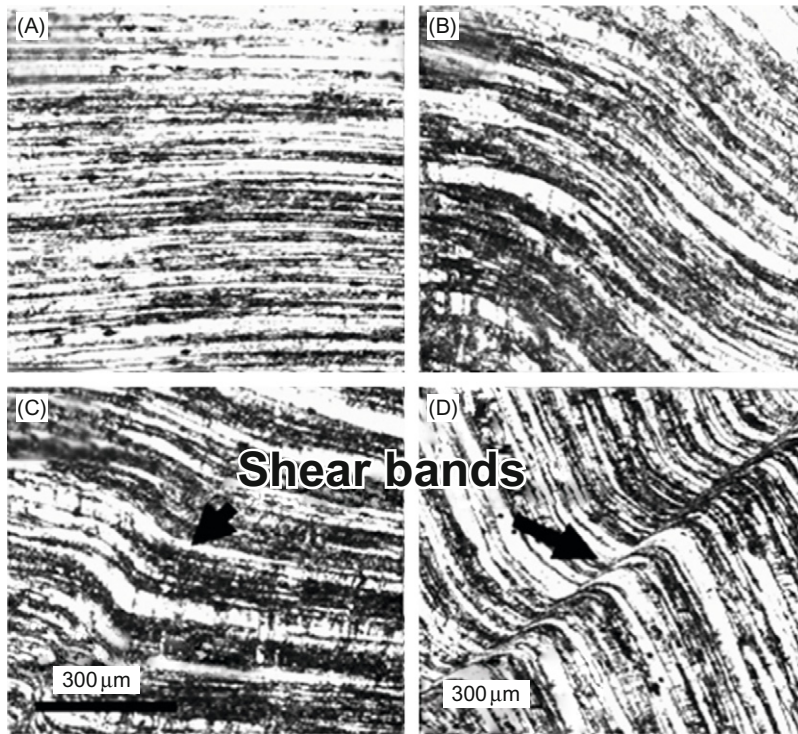
f0015 **Figure 3.2** Evolution of localized deformation in Al−Li alloy subjected to dynamic impact compression [56].

the cross section of the specimen, implying that the specimen is still work hardening. However, as the average strain increases from 0.10 to 0.17, corresponding to a loading time of 80 μs, localized deformation starts to occur (Figure 3.2B). Beyond this point, the specimen appears to work soften as the loading time increases, and localized deformation becomes more apparent as shown in Figure 3.2C. When the loading time is ∼120 μs, the shear band with a width of 25 μm is shown in Figure 3.2D. It is clear that the evolution of localized deformation is a rapid progressive process during which the localization becomes more apparent, and the width of the band becomes gradually narrower.

s0025 ## 3.4 Conditions Required for Shear-Band Formation

p0295 Determining the criteria for shear-band formation has been one of the most interesting research challenges. For more than three decades, approaches have been

focused on theoretical treatments, which consist of a combination of mechanical instability analysis with a thermal model. These analyses generally concur that after the critical strain corresponding to the macroscopic maximum in load on a stress−strain curve of the material has been achieved, the shear bands form. Based on the thermoplastic instability in simple shear, Bai [4] and Timothy et al. [57] carried out the linear perturbation analysis and suggested a maximum load required for the formation of the shear bands. Molinari [58] provided a more advanced non-linearized perturbation analysis. Wright [59] extended this treatment and proposed a double instability/localization criterion. In this criterion, the maximum in the load corresponded to the instability. Localization was a separate event that followed instability. The strain between the two could be significant. Staker [60] examined the effect of the steel-tempering temperature on the susceptibility to transformed band formation. He proposed that there exists a critical strain for the formation of the transformed bands that depends on the heat-treatment condition of the steel. Taking thermal softening and conduction into account, Recht [2] proposed a critical strain rate as a criterion for the occurrence of the shear band. Rogers [14] pointed out in his review that 'the above results bear on the problem of whether or not a "critical strain rate" exists for adiabatic shearing in a given material'. He pointed out again that 'Large strain can be achieved quasi-statically in steel without transformed band formation; hence, provided that a minimum strain achieved, there must exist a strain rate above which the removal of heat from the region of deformation is sufficiently limited that the temperature can rise above that needed for transformation to occur − a critical strain rate'. Zurek [61] found that the average strain of 0.5 and the associated average strain rate of $1.8 \times 10^4 \, \text{s}^{-1}$ were sufficient to induce an adiabatic shear instability in 4340 steel, implying that both strain and strain rate should be required for white etching band formation. Bai [62] has proposed a criterion describing possible instability in simple shear deformation combining thermal softening, current stress, density, specific heat, work hardening, thermal conductivity and current strain rate implying that the condition for band formation should include both the stress and strain rate. This is verified by the experimental results of the aluminium and titanium alloys [56,63].

AU : 10

p0300   Figure 3.3 shows two types of bands formed in an aluminium−lithium alloy subjected to dynamic impact compression. It reveals that as the strain rate increases, localized deformation develops gradually, and when the strain rate reaches $1.75 \times 10^3 \, \text{s}^{-1}$, the deformed shear bands appear first as shown in Figure 3.3A, and as deformation proceeds, the width of the band becomes gradually narrower. When the strain rate is $\sim 2.0 \times 10^3 \, \text{s}^{-1}$, the white bands occur (Figure 3.3B). The results measured are listed in Table 3.2 [56]. The critical strain is 0.14 for deformed band formation, at a given strain rate ($1.6 \times 10^3 \, \text{s}^{-1}$). As the strain increases from 0.14 to 0.17, a white etching band appears. This result is verified by Li et al. [66]. They found that the shear bands began to form when both strain and strain rate reached the critical values of 23% and $2.8 \times 10^3 \, \text{s}^{-1}$, respectively.

AU : 11
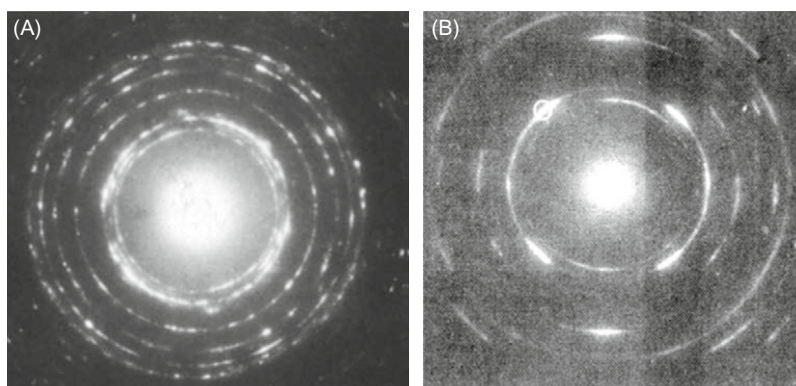
f0020 **Figure 3.3** (A) First diffraction pattern from the Ti−4Al−4V shear band; specimen shows appearance of transformed band, but the diffraction pattern indicates breakup of microstructure [64] and (B) first diffraction pattern from Ti showing arced circles characteristic of ultrafine-grained size [65].

Table 3.2 Critical Strain and Strain Rate for Shear-Band Formation in Al−Li Alloys [56]

	Peak-Aged Alloy	Underaged Alloy
Strain rate (s^{-1})	1,600	2,000
Critical strain for deformed band	0.14	0.17
Critical strain for white etching band	0.17	0.21

s0030 ## 3.5   Deformed and Transformed Bands

p0305 The shear bands have been classified into deformed bands and transformed bands, on the basis of their appearance in the metallographic section. The transformed band is also often referred to as a white etching band or white shear band in steels and has received much attention because it was suggested that the phase transformation temperature is reached in the band, supporting the thermoplastic instability theory of shear localization. The white etching bands have been reported mainly in steels [1,61,67−70], titanium and titanium alloys [22,23,30,71], aluminium alloys [56] and magnesium alloys [72].

p0310   The evidence for occurrence of phase transformation in the bands in steels seems to rise from the white etch in a nital, a well-defined width, distinct boundaries between the band and the matrix and very high hardness. Trent [73] made the earliest observation of the white etching bands in steel and found that these bands appeared to be white or slightly yellow on the sheared surface. He attributed to the occurrence of deformation-induced transformation. Some investigators refer to it as

a dislocation cell structure, while others refer to it as consisting of extremely fine grains [69,74]. Zener and Hollomon [1] assumed that the white etching band was caused by a rapid quenching from the high temperature. Scott et al. [74] pointed out that the white etching bands could not show the tempering characteristics of conventional martensite, even when heated to temperatures above normal tempering temperatures. Heating to above the austenite temperature, however, could cause a disappearance of the white etching bands and the formation of a structure indistinguishable from the remainder of the specimen. Based on the selected area electron diffraction (SAED) analysis, they suggested that the white band was supersaturated ferrite. Further investigations by TEM and X-ray show that the band area was a typical looking martensite [69], a fine-grained equi-axed delta ferrite and a martensite with carbides [27] and untempered martensite [1]. TEM examinations by Beatty et al. [75] demonstrated that the shear-band region was ferrite with the nanograins. We now know that the white etching effect and the high hardness can be caused by the formation of an ultrafine-grained structure, which can, by virtue of the Hall−Petch effect, reach higher levels than the surrounding matrix that is deformed homogeneously. However, phase transformations can and do occur, and the resulting phases in the shear bands are the result of the following:

u0055 • Thermodynamics of phase stability
u0060 • Kinetics of phase transformations
u0065 • Shear deformation effect, introducing high densities of defects.

p0330   For instance, one of the first observations of deformed and transformed bands, by TEM, is by Me-Bar and Shechtman [64]. (The latter is the 2011 recipient of the Chemistry Nobel prize for his discovery of quasi-crystals.) Figure 3.3A shows the diffraction pattern in a deformed band, which clearly shows the ringed and arced appearance that was later attributed to an ultrafine-grained structure. The spots are clear and sometimes smeared, evidence of deformed grains and a small grain size. Similar results were obtained by Grebe et al. [65] in commercially pure titanium. They identified the grain structure as equi-axed grains with approximate diameter of 300 nm. It is interesting that, upon observation in optical microscopy, the bands in Ti give the appearance of being 'transformed'. Grebe et al. [65] indexed the rings in Figure 3.3B to the hexagonal structure. Thus, no transformation was obtained.

p0335   When discussing the phase transformation in the band, the critical role of the temperature rise in transformation should be mentioned. A number of authors proposed that the maximum temperature during localized shearing may reach several hundred degrees above that of the surrounding matrix. This is usually inferred indirectly from metallurgical evidence, and the shear band is then proposed to be rapidly cooled by the surrounding bulk material when plastic deformation ceases, and cooling rates as high as 10^7 K/s have been calculated [22]. However, some measurements have been made directly [21,24,30]. These authors used the IR detection system to determine that the temperature distribution of the band region was in the range of 440−550°C for the Ti−6Al−4V [30] and 450−590°C for steel [23,30]. They concluded, therefore, that there was no clear evidence to suggest that the

AU : 12

f0025
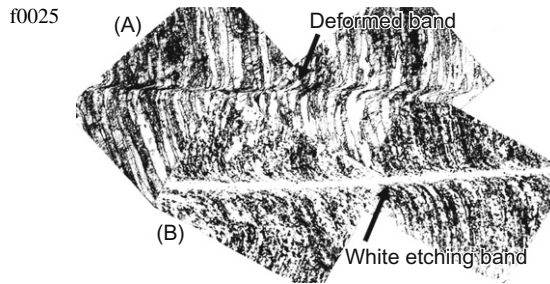
Figure 3.4 The deformed and white etching bands generated during dynamic impact compression testing in Al−Li alloy [71].
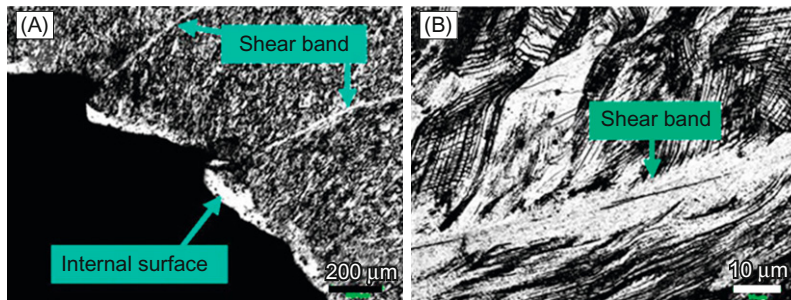

f0030 **Figure 3.5** White etching bands in 304 stainless steel imaged by CLSM at low (A) and high (B) magnifications [19].

material within the band had undergone a phase transformation. Giovanola [52] pointed out that there is no conclusive direct evidence for occurrence of phase transformation in the white bands. The only important point of common agreement is that the structure in the white bands is composed of very fine grains. Rogers [14] mentioned that 'whether there is a single crystallographic structure for the trans- AU : 13 formed bands in steel or whether there are a variety of structures dependent on the particular material and the deformation condition is still a very open question. In addition to etching behaviour, there are two almost universally recognized characteristics of the transformed bands in steels: their very high hardness and their extremely fine structure. The investigation made in Al−Li alloys has shown that deformed bands form first (Figure 3.4A), corresponding to a critical strain of 0.14, and as deformation proceeds, localization gradually becomes apparent. Finally, a white etching band occurs on the base of the deformed band corresponding to a critical strain of 0.17 (Figure 3.4B). Timothy [15] pointed out that the formation of a 'transformed' band appears to correspond to an advanced stage of adiabatic strain localization in a given metal, with a deformed band representing an earlier stage in the process. The results mentioned here are supported by the recent result in high-speed machining of the high-strength steel [76].

p0340   A number of investigations have shown that whether the bands are deformed or transformed, their presence is generally indicated by the different etching responses in the band of material in metallographic cross sections. Figure 3.5, imaged by
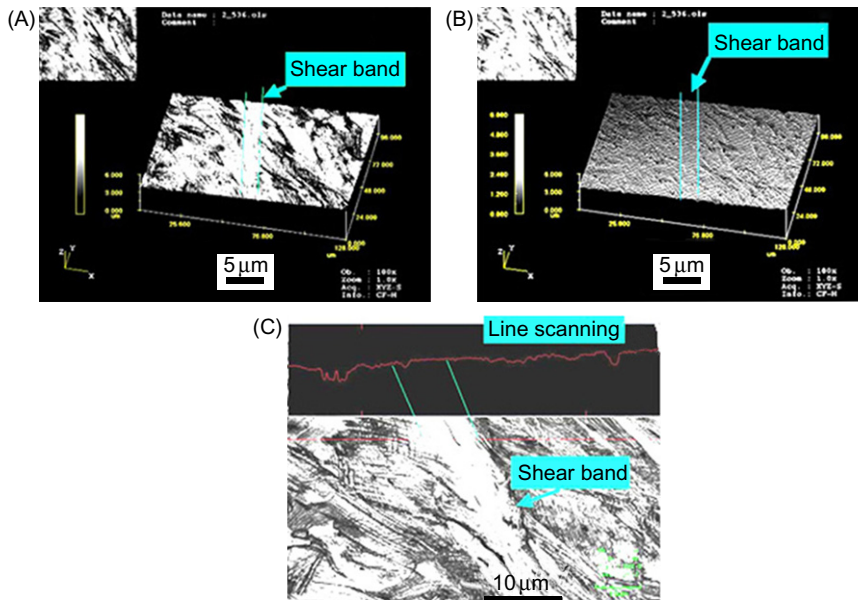
f0035   **Figure 3.6** The shear bands imaged by CLSM: (A) scanning mode, (B) profile scanning and (C) line scanning across the band [19].

confocal laser scanning microscopy (CLSM), shows the white shear bands in 304   AU : 14 stainless steel subjected to explosive collapsed testing. One of the possible reasons for the 'white' colour of the band is the occurrence of a martensite that is too hard to be etched, causing the white colour (the α'-martensite phase transformation does occur in the band; this will be shown in Section 3.6). To verify this, profile line scanning across the band was performed by CLSM. If the band is lightly etched, then the profile-scanning line should appear to be a protrusion when the scanning is across the band (Figure 3.6). The profile scanning is selected along the horizontal line (Figure 3.6C). The line does not appear to be a protrusion, implying that the structure in the band is not difficult to etch. EBSD analysis shows [77−79] that the structures in the band undergo intensive localized deformation with large strains and super high-strain rates, forming substructures highly elongated along the band direction; these substructures form low-angle boundaries of about 2−15° in misorientation. This is proposed to be the possible reason for the white colour of the band. In other words, the white etching band is an unlikely indication of the phase transformation; in fact, the observed substructures in the white etching bands differ by a degree not observable by ordinary optical microscopy or by SEM. Both the ordinary light and secondary electron wave could not 'see' the substructure difference in orientation in the bands. Therefore, the band appears to be white when viewed by ordinary light under optical microscope or secondary electron wave in SEM. So it is reasonable to propose that the white etching is unlikely to be the
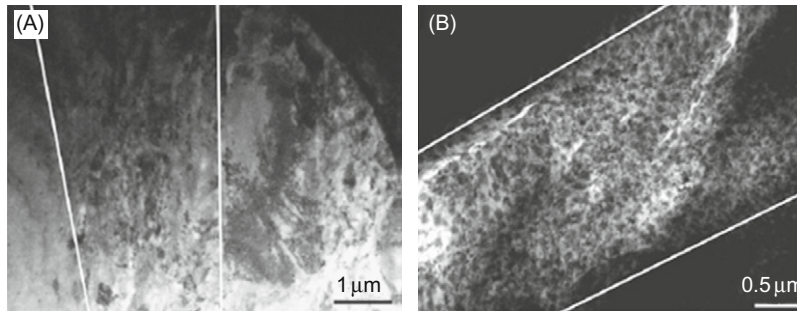
f0040 **Figure 3.7** Adiabatic shear bands in magnesium alloy AM60B target impacted by steel projectile at a velocity of 0.5 km/s: (A) deformed bands and (B) 'transformed' bands. Boundaries of bands are marked by white lines.
Source: From Ref. [72].
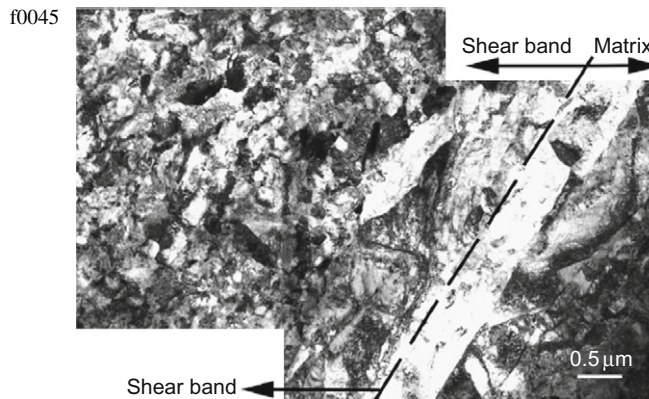
f0045

Figure 3.8 Shear band (left), matrix (right) and the matrix/shear band (dashed region) interface for Zircaloy deformed in a hat-shaped geometry. The interface between adjacent regions is sharp.
Source: From Ref. [76].

occurrence of phase transformation in the bands. This analysis is verified further by EBSD studies in Fe−Cr−Ni monocrystal and 304 stainless steel [77−79].

p0345   The recent results obtained by Zou et al. [72] on magnesium alloys confirm the generality of the structures in shear bands. There is a critical strain above which the structure reorganizes itself into nanometre or ultrafine-grain sizes. In the case of the AM60B magnesium alloy, the grain size in the 'transformed' band is in the range of 50−100 nm. This is shown in Figure 3.7. Figure 3.7A shows the band that is called 'deformed' and shows the effect of deformation. On the other hand, in Figure 3.7B, for a larger strain, the deformed structure is replaced by one consisting of nanosized grains. This structure is called 'transformed', but the only transformation it underwent is the size and configuration of the grains. Zou et al. [72] observed the characteristic increase in hardness, but it is due to the reduction in grain size. The structure of the nanocrystalline shear band remains hexagonal. Figure 3.8 shows the same phenomenon in Zircaloy [80]. The structure inside the

shear band, on the left side, consists of ultrafine grains with ~ 200 nm diameters. The interface between band and surrounding material is clear.

p0350   Recent investigations have shown, however, that phase transformation can occur in both the deformed and transformed bands; this will be described in the following section.

s0035 ## 3.6 α'-Martensite Transformation in Shear Bands

p0355 Recent studies have shown that the phase transformation does occur, certainly in the shear bands in 304 stainless steel [32], Fe−Cr−Ni monocrystal [20] and Ti−6Al−4V alloys [81]. Figure 3.9 is a shear band, and its microstructure observed in 304 stainless steel is subjected to the cylindrical collapse (TWC) test with a strain rate of 10^4 s^{-1}. Figure 3.10 is the TEM image taken from a field in the band shown in Figure 3.9, indicating that a α'-martensite transformation occurs. This kind of phase transformation particularly generates at the intersection between the shear band and twins. Further analysis shows that the $(\bar{1}10)$ planes of the α'-martensite are coherent with the $(\bar{1}11)$ planes of the parent austenite and parallel to each other. The direction, [110] of the α'-martensite, is parallel to the [211] of the austenite [32], e.g. (1 1 0)$_{\alpha'}$ // (1 1 1)$_\gamma$;[0 0 $\bar{2}$]$_{\alpha'}$ // [0 2 $\bar{2}$]$_\gamma$;[$\bar{1}$12]$_{\alpha'}$ // [1 3 1]$_\gamma$; [1 1 0]$_{\alpha'}$ // [211]$_\gamma$, which is in accordance with the Nishiyama orientation. From this, it is concluded that the (110) of the α'-martensite nucleates along the {111} of the austenite. Essentially, these results confirm earlier investigations made by Staudhammer et al. [82] in dynamic tensile testing of the same materials. These α'-martensite laths nucleate preferentially at twin-band intersections in the area of localized strain. They have been identified by Murr et al. [83] and Kestenbach et al. [84] in connection with shock compression. These are the twinning and slip planes, and, thus, their intersections provide the nucleus [85]. A similar phase transformation was also observed in the shear bands in Fe−15%Cr−15%Ni monocrystal subjected to the dynamic explosive loading [20,86].

p0360   Figure 3.11A is a bright-field image taken from a primary α-grain in the band of the Ti−6Al−4V alloy, and Figure 3.11B is its combined electron diffraction pattern. Figure 3.11C and D shows the bright-field and dark-field images obtained
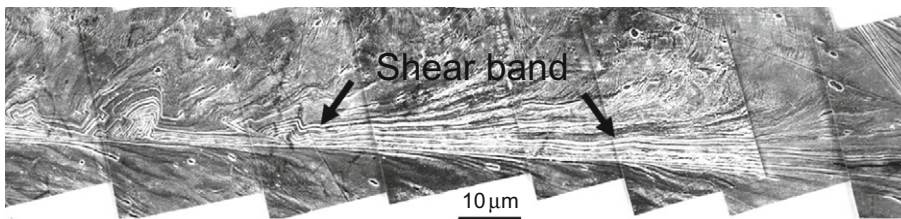

f0050 **Figure 3.9** Shear band generated in cylindrical collapsed specimen of 304 stainless steel subjected to global $\varepsilon_{\mathrm{eff}} = 0.92$ [32].   AU : 62
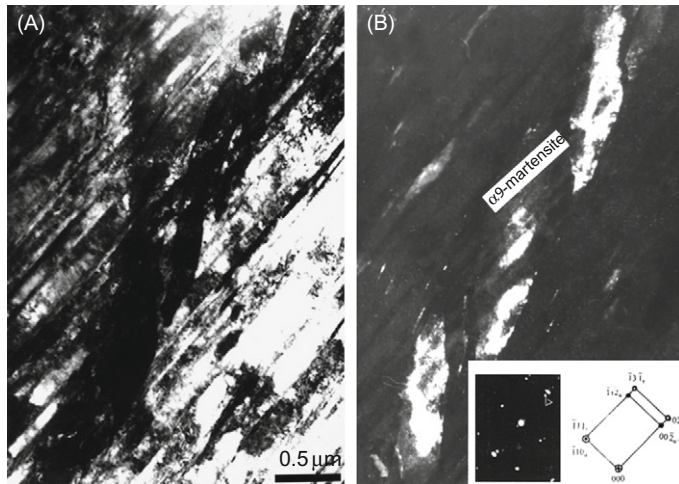
f0055 **Figure 3.10** TEM bright-field (A) and dark-field (B) images, showing α'-martensite phase transformation formed at the intersection between the twins and the shear bands in 304 stainless steel subjected to explosive collapsed testing [32].
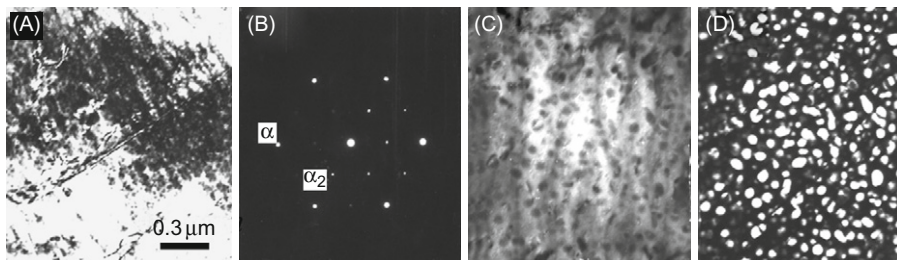
f0060 **Figure 3.11** TEM montage, showing bright-field images (A) of the high-strain-rate deformation structure in Ti−6Al−4V alloy, and its [0001] zone axis diffraction pattern (B), and dark-field images obtained by using strong diffraction spots $\{2\bar{2}00\}_{\alpha}$ and weak super-lattice reflection $\{1\bar{1}00\}_{\alpha 2}$, respectively [71].

by the strong diffraction (α) and the weak super-lattice reflection $\{1\bar{1}00\}_{\alpha 2}$, respectively. Analysis shows that the α_2 phases (Ti$_3$Al) are proposed to be transformed from the α-matrix, and both the α_2 phases and α-matrix are completely coherent [71].

p0365   An interesting observation by Wang et al. [87] in a Ti−3Al−5Mo−4.5V alloy in the two-phase α-β microstructure is that the α phase recrystallized into ultrafine grains, whereas the β phase, passing the transformation temperature, recrystallized into an α' structure. The β phase disappeared inside the alloy. This is additional
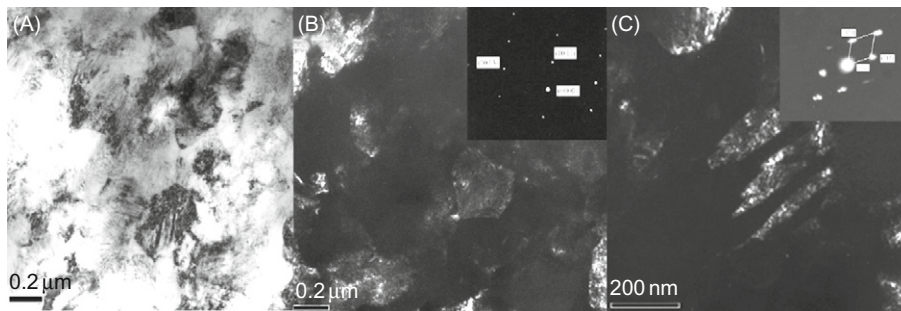
f0065 **Figure 3.12** TEM micrographs and SAD patterns showing the microstructure in the centre of a shear band in a TiAlMoV alloy initially in the two-phase α-β structure: (A) and (B) are the light-field pattern of the microstructure in the centre of the shear band, and (C) and (D) are the dark-field patterns and their corresponding SAD patterns of α phase and α' phase in (A) and (B), respectively.
Source: From Ref. [87].

evidence that phase transformation can occur in conjunction with recrystallization. The bright-field and dark-field TEM micrographs together with diffraction patterns are shown in Figure 3.12.

s0040 3.7   Effect of the Microstructures on the Tendency for Localized Shear Bands

p0370 It is generally accepted that a material will be sensitive to localized shearing if it is characterized by a low strain hardening, a low specific heat and a high thermal softening. This was implicit in the first analysis carried out by Zener and Hollomon [1]. Rogers [14] pointed out that the deformed bands are likely to form in iron and carbon steels when the structure is coarse. Also, as the rate of deformation decreases, there is a greater tendency for the shear bands to be of the deformed type and a transformed portion to extend from the region of the most intense shear to a point at which the local temperature has not exceeded the transformation temperature. Costin et al. [88] found that shear bands developed in all high strain-rate tests with cold rolled steel and that none formed in hot rolled steel when deformation was limited to about 30% strain. These steels showed very similar strain-rate sensitivities and thermal softening rates. Shawki [89] predicted that the shear bands would form in hot rolled steel, deformed dynamically if a nominal strain of 80−100% was imposed; they considered that the reason for the absence of localized shear in the hot rolled steel could be attributed to the low strain used. This proposal was justified by the results of Hartley et al. [51]. However, they found that the shear bands in hot rolled steel are narrower than that in cold rolled steel.
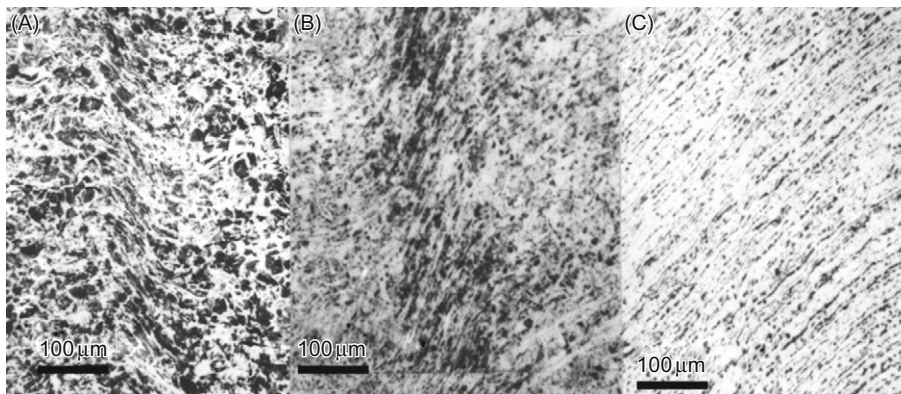
f0070 **Figure 3.13** Shear bands in the low-carbon steels: (A) quenched condition, (B) quenched and tempered and (C) normalized [26].

Table 3.3 Mechanical Properties and Structural Parameters of the Steels Tested [26]

Microstructure	σ_f (MPa)	n (s^{-1})	γ	γ_c	W_m (μm)	ΔT (°C)
F + M$_q$	699	0.179	650	0.30	75−100	210
F + M$_p$	649	0.180	610	0.36	130−150	265
F + P	498	0.22	1,500	0.83	350−400	275

σ_f, fracture strength; n, work hardening; γ, strain rate; γ_c, average critical strain; W_m, width of the band; ΔT, the rise in temperature in the band.

Xu et al. [26] studied the tendency of the low-carbon steels with different structures to shear localization and found that the critical strain required for the occurrence of shear localization is strongly dependent on the strength of the steels at a given strain rate. Figure 3.13 shows that the critical strain values required for the shear-band formation for the quenched, quenched and tempered and normalized steels are 0.30, 0.36 and 0.83, respectively, implying that the steel with quenched martensite is most susceptible to shear deformation. The higher the strength of the steels, the easier it is for the band to occur (Table 3.3). The quenched steel with high strength and low work-hardening capability does develop a pronounced band with a width of 70−100 μm (Figure 3.13A). However, the width of the bands in the normalized steel with higher capability of the work hardening is much larger than those of the other two steels, ∼350−400 μm (Figure 3.13C). The width in the quenched and tempered steel is in between them (Figure 3.13B). It should be pointed out that the boundary between the bands and the matrix for these steels is not well defined.

p0375 One more example is shown in Figure 3.14, displaying the effect of the micro-structure on the tendency for shear deformation in an aluminium matrix composite reinforced with different sized SiC particles [90]. It is found that the composite
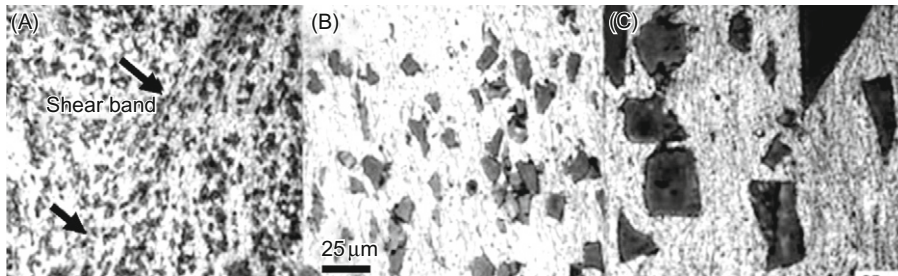
f0075   **Figure 3.14** Deformation pattern in Al-17% SiCp composite with an average particle size of 3 μm (A), 13 μm (B) and 17 μm (C) produced during high-strain-rate loading. Note that material with smaller particles (3 μm) develops a well-defined localized shear band (A), and shear localization in the materials with larger particles (13 and 17 μm) does not develop well (Figure 3.10B and C).

reinforced with smaller particles (3 μm) develops well-defined shear bands as shown in Figure 3.14A, and those with larger SiC_p of 13 (Figure 3.14B) and 17 μm (Figure 3.14C) in size tend to deform inhomogeneously, so localized shear was not well developed. This implies that the particles may play a significant role in formation and development of shear localization, and the smaller the particles in size, the easier the shear-band formation, which coincides with the results obtained by Lee et al. [91]. The tendency of the composite reinforced with small particles to form shear localization is greater than that of the other two materials with large particles, when the volume fraction of the particles in the composite remains the same. This size-dependent deformation localization behaviour of particle-reinforced metal-matrix composites is confirmed by recent research results [92]. In Chapter 7, S.   AU : 15 Walley discusses shear localization in granular materials. Shih et al. [93] studied shear localization in granular SiC and observed the fragmentation of the material within the shear bands. The existence and propagation of strain in shear bands benefits from small particles, smaller than the width of the shear band.

s0045   ## 3.8   Crystalline to Amorphous Transition Within Shear Bands

p0380   Figure 3.15B shows a bright-field image taken from an area of the shear band (Figure 3.15A) observed in Fe−Cr−Ni single crystal subjected to the cylindrical collapse (TWC) test with a strain rate of $10^4 \, s^{-1}$. It is seen that both amorphous and nanosized grain regions can be recognized. The amorphous area is absent from the crystalline lattice, and the corresponding diffusion halo-ring (insert) and its radius coincides with that of a Fe−Cr−Ni single crystal. On the other hand, the combined diffraction pattern consists of the spots and rings (insert), indicating
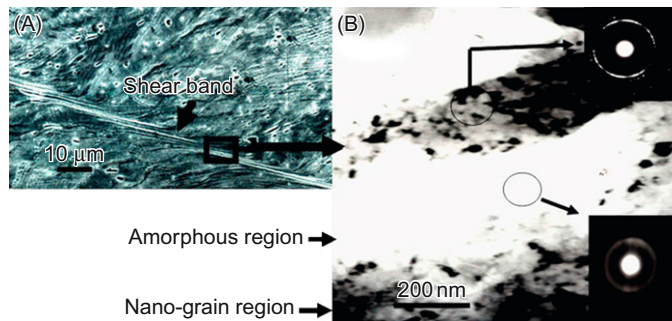
f0080 **Figure 3.15** The shear-band pattern (A) and a bright-field image taken from a square in the band (B).


f0085
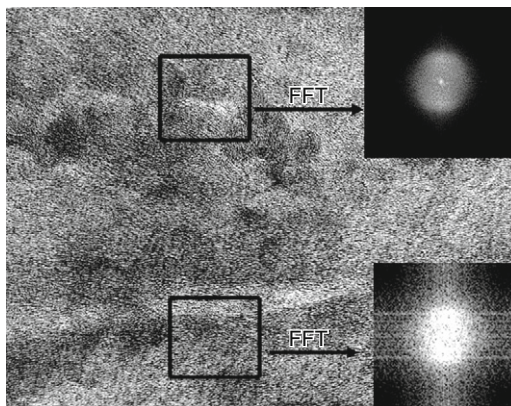
Figure 3.16 HREM image from the amorphous region, and the FFTs performed on different areas marked by squares.

occurrence of the nanosized grains. Figure 3.16, an HREM image from the amorphous area, shows disordered lattice, which is verified further by fast Fourier transformation (FFT) (inserts) from different areas marked by the squares showing also the absence of crystalline lattice. These provide strong evidence for the lack of crystalline symmetry in the shear band induced during dynamic deformation for this material.

p0385   The images of TEM (Figure 3.17A) and HREM (Figure 3.17B) from the ultra-fine-grained region of the band in Figure 3.15 show the nanograins clearly. EBSD was used to characterize the microstructure inside the band. Figure 3.18A and B shows Euler maps, and Figure 3.18C is a Kikuchi contrast taken from the band shown in Figure 3.15A. It is clear that in addition to equi-axed recrystallized grains, the area in blue is not resolved, which implies the absence of the crystalline lattice symmetry [94]. These results are supported for the first observation by Meyers et al. [32], cornering the crystalline to amorphous transition in bands in 304 stainless steel

AU : 16
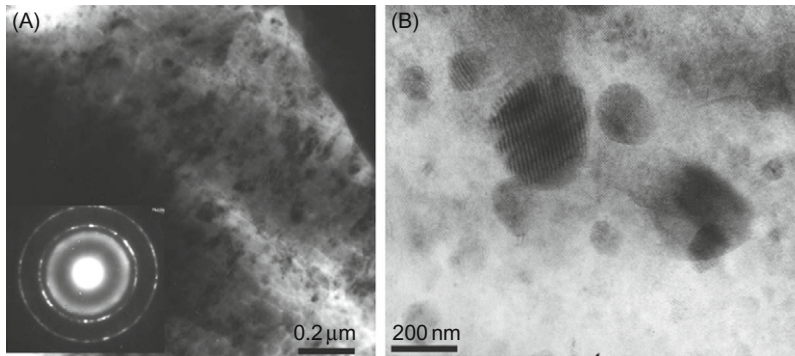
f0090   **Figure 3.17** Images from the nanosized grain region by TEM (A) and HREM (B).

f0095
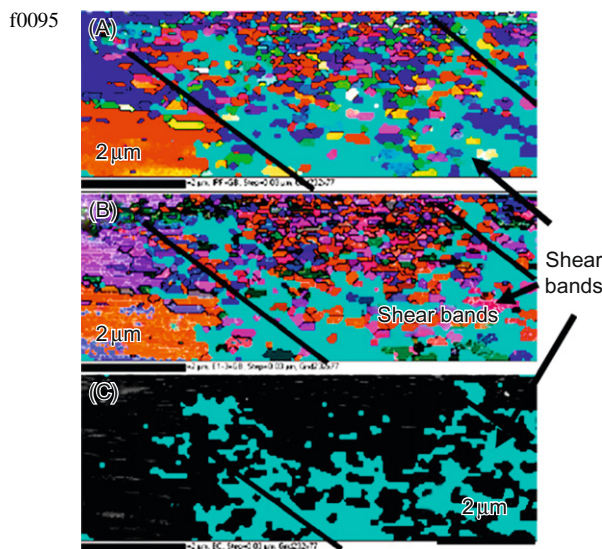
Figure 3.18 Euler maps (A and B), and Kikuchi contrast (C) obtained in the shear band.

under dynamic deformation, and further verified by the more recent work of Li et al. [95], and they have found the coexistence of both amorphous and nanocrystalline phases in a shear band in TWIP steel subjected to ballistic impact with a high strain rate of $\sim 10^5 \, \mathrm{s}^{-1}$ as shown in Figure 3.19.

AU : 17

p0390   One of possible reasons for this arises from either the surface contamination or unfairness of the sample tested. In fact, the occurrence of the equi-axed grains in the same area as that in blue (Figure 3.18) implies that surface contamination or unfairness of the sample is ruled out. From these analyses, it is reasonable to propose that the transition of crystalline to amorphous structures within the bands can occur during dynamic deformation.
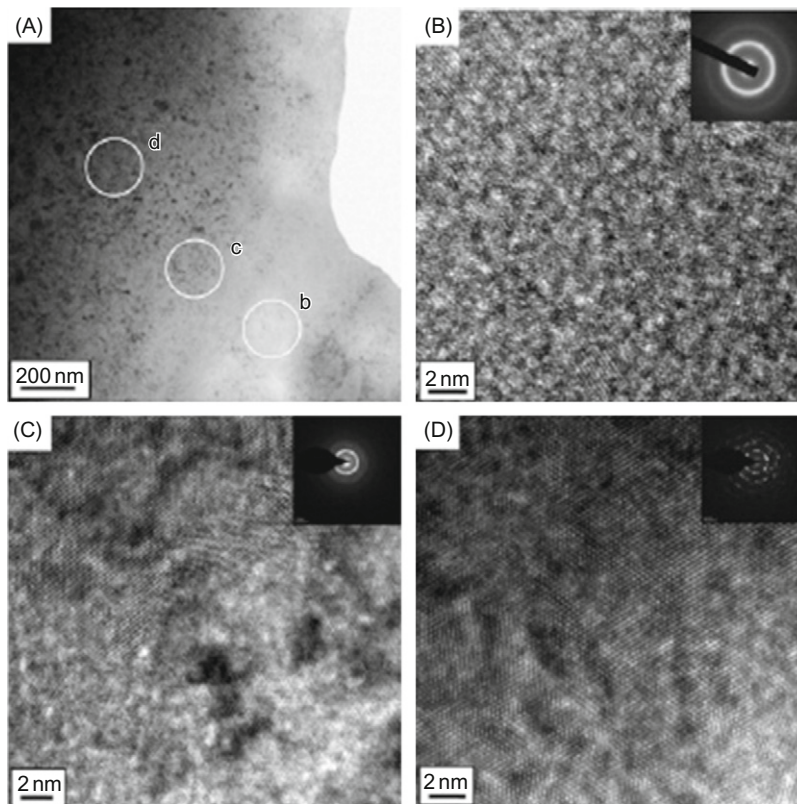
f0100   **Figure 3.19** Bright-field image (A) from a shear band in TWIP steel, and HREM images showing the amorphous phase (B), the transition region of crystalline to amorphous (C) and nanocrystalline (D).
Source: From Ref. [95].

s0050   ## 3.9   Static/Dynamic Recrystallization

s0055   ### 3.9.1   Observations by EBSD

p0395   Recrystallization in the shear bands arising from high-strain-rate loading has been documented well and reported in steels [32,96,97], in titanium [98], in copper [99,100] and in tantalum [101,102]. It is generally accepted that the deformation and associated temperature rise in the band are therefore sufficient to induce new recrystallized grains. Figure 3.20A shows the nanograins with an average size of 100 nm in diameter in the band of 304 stainless steel. The large grains outside the band with about 50–100 μm in diameter are also shown (Figure 3.20B). Recently, EBSD has been used to characterize structures in shear bands in steel [77–79,97] and Ti alloy [103]. Figure 3.21 shows the Euler (A) and Kikuchi (B) contrasts and
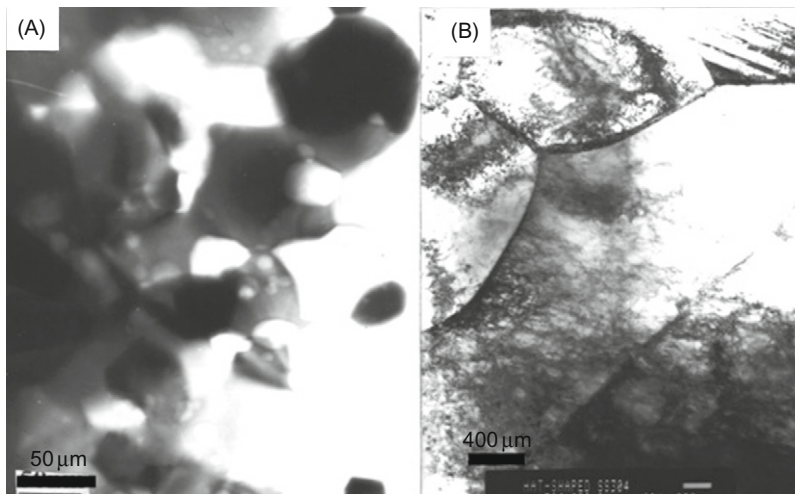
f0105   **Figure 3.20** Nanograins (50−100 nm in diameter) inside (A) and large grains (50−100 μm) outside (B) bands [32].

the pole figure (C) contrasts of Fe−15%Cr−15%Ni monocrystal, respectively [77]. A band that is 2 μm wide and a great number of distortion-free and equi-axed grains are apparent. This type of equi-axed structure is proposed to be the result of the occurrence of static recrystallization in the band [79]. The pole figures (Figure 3.21C) obtained in a region crossing the band show that the orientation ($<100>$) of the red area outside the band is in good agreement with that of the starting single crystal orientation ($<100>$). The substructures (in orange) below the band have an orientation ($<111>$) that is parallel to ND in the {111} pole figure, and the substructures (in red) have an orientation ($<100>$) that is parallel to ND, therefore, $<111> // <100>$. However, misorientation between them (in orange and blue) is typical of low-angle boundaries (1−3°) [81]. The average size of the grains in the band determined by linear intercept is about 200 nm. A similar structure has also been observed in the band of 304 stainless steel as shown in Figure 3.22 [81]. From these observations, you can see that the grains in the band are basically equi-axed, implying that these new recrystallized grains grow isotropically, after nucleation, and they are no longer oriented along the shear deformation direction. It is reasonable to propose, therefore, that the equi-axed grains in the band should be the result of static recrystallization. Recent observations show that another mechanism of recrystallization in the band operates in Fe−Cr−Ni monocrystal as shown in Figure 3.23. By comparing Figure 3.23 with Figures 3.21 and 3.22, it is seen immediately that the grains shown in Figure 3.23 are not equi-axed but elongated along the shear direction [78]. This indicates strongly that after nucleation, the nuclei of the new recrystallized grains grow preferentially under the stress along the shear direction. In other words, these elongated grains
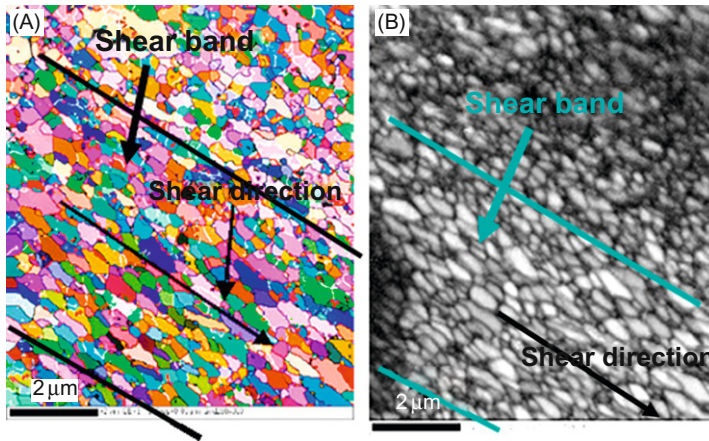
AU : 18
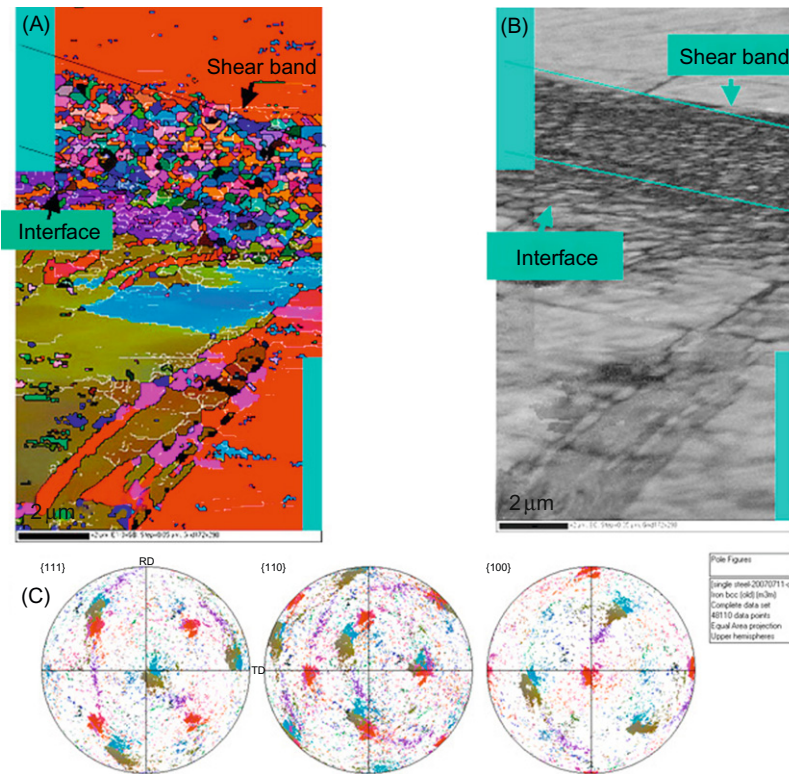
f0110 **Figure 3.21** Euler (A) and Kikuchi (B) contrast and pole figure (C) of Fe−15%Cr−15%Ni monocrystal subjected to explosive collapsed loading [77].
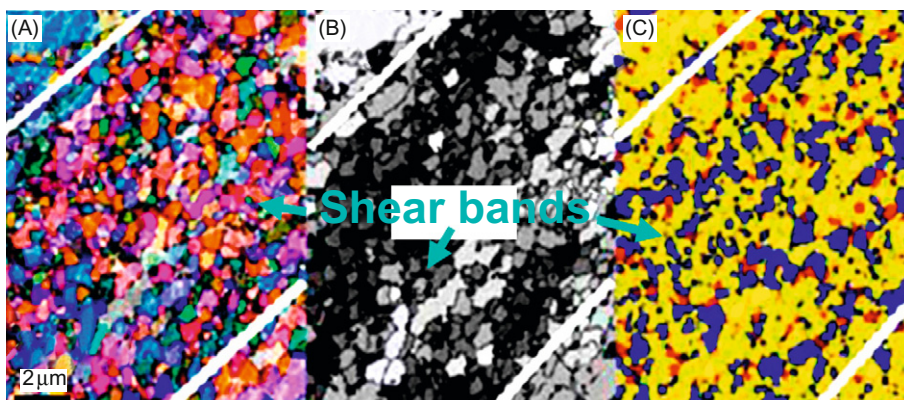
f0115 **Figure 3.22** EBSD maps inside a band in 304 stainless steel: (A) Euler contrast map, (B) Kikuchi contrast map and (C) deformation map showing the equi-axed recrystallized grains in the band [81].

f0120   **Figure 3.23** EBSD maps of recrystallized grains in the band in Fe−Cr−Ni monocrystal subjected to explosive collapsed loading: (A) Euler and (B) Kicuchi contrasts [78].

along the shear direction were developed simultaneously with localized deformation, and, therefore, these elongated grains are proposed to be dynamically recrystallized [78].

s0060   ### 3.9.2   Analysis of Microstructure Evolution

s0065   *Grain-Boundary Rotation*

p0400   Meyers et al. [104] proposed a grain-boundary rotation mechanism to describe the process of recrystallization occurring during deformation. For this mechanism to be viable, it has to be shown that grain-boundary rotation can be accomplished within the time/temperature window created by plastic deformation. The relaxation of the rotated grains into a more equi-axed micro-crystalline structure can occur by minor rotations of the grain boundaries. This is shown in Figure 3.24A, where it is shown that a rotation of 30° of the boundaries transforms elongated segmented subgrains into an equi-axed structure. If each longitudinal grain-boundary segment rotates by an angle θ, the equi-axed structure will be created. This can be accomplished by the flux of atoms along the grain boundary, which can occur at rates that are orders of magnitude higher than in the bulk. A general form of Fick's law expressed in terms of a potential energy gradient must be used [105]. This is a critical element of the model: a mechanical stress induces diffusion. We start with force $\vec{F}$, acting on a particle,

$$\vec{F} = \nabla V \tag{3.1}$$
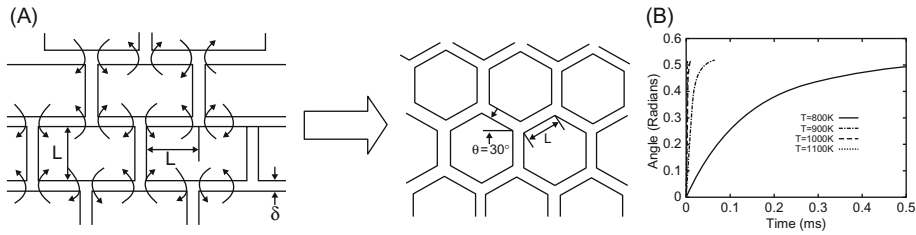
f0125 **Figure 3.24** (A) Representation of the rotational recrystallization mechanism leading from elongated subgrains to equi-axed ultrafine grains through rotation of grain boundaries. (B) Calculated rotation of boundaries (from a grain size of 100 nm as a function of time for three temperatures) [19,98].

where ∇V is the gradient of the potential energy field. The mean diffusion velocity $\vec{v}$ is the product of the mobility M by this force: $\vec{v} = M\vec{F}$. The flux along a grain boundary with thickness δ and depth L_2 (cross-sectional area $L_2\delta$) is

$$J = L_2 \delta CMF = \left(\frac{L_2 \delta DC}{kT}\right) F \tag{3.2}$$

where D is the diffusion coefficient and C is the concentration of the mobile species (expressed in terms of mass per unit volume).

p0405 The rotation of the boundaries is driven by the minimization of the interfacial energy [106]. The force exerted by the grain boundaries is equal to

$$F = \gamma \left(1 - 2\cos\frac{\theta_3}{2}\right) L_2 \tag{3.3}$$

The relationship between the grain-boundary rotation and the volume flow, dV, is (this is computed per thickness, L_2)

$$\frac{L^2 \, d\theta}{4L_2} = dV \tag{3.4}$$

where dV is the volume transferred and L is the instantaneous length of the segment. However,

$$L = \frac{L_1}{\cos\theta} \tag{3.5}$$

where L_1 is the initial length. Thus,

$$\frac{\mathrm{d}\theta}{\mathrm{d}t} = \frac{4\cos^2\theta}{L_2L_1{}^2}\frac{\mathrm{d}V}{\mathrm{d}t} = \frac{4\cos^2\theta}{L_2L_1{}^2\rho}\frac{\mathrm{d}m}{\mathrm{d}t} \tag{3.6}$$

where $\mathrm{d}m/\mathrm{d}t$ is the mass change, which is the rate of volume change multiplied by ρ, the density.

p0410   The rate of mass change is the flux, and we have, substituting Eq. (3.2),

$$\frac{\mathrm{d}\theta}{\mathrm{d}t} = \frac{4\cos^2\theta}{L_2L_1{}^2\rho}J = \frac{4\cos^2\theta}{L_2L_1{}^2\rho}\left(\frac{L_2\delta DC}{kT}\right)F \tag{3.7}$$

$$\frac{\mathrm{d}\theta}{\mathrm{d}t} = \frac{4\cos^2\theta}{L_1{}^2\rho}\frac{\delta DC}{kT}\gamma(1-2\sin\theta)L_2 \tag{3.8}$$

p0415   We consider equi-axed grains and $L_2 \approx L_1$:

$$\frac{4\delta D\gamma}{L_1 kT}t = \int_0^\theta \frac{\mathrm{d}\theta}{\cos^2\theta(1-2\sin\theta)} \tag{3.9}$$

p0420   Integrating, we arrive at an expression,

$$t = \frac{L_1 kT}{4\delta D\gamma}f(\theta) \tag{3.10}$$

where

$$f(\theta) = \frac{\tan\theta - \frac{2}{3}\cos\theta}{(1-2\sin\theta)} + \frac{4}{3\sqrt{3}}\ln\frac{\tan\frac{\theta}{2}-2-\sqrt{3}}{\tan\frac{\theta}{2}-2+\sqrt{3}} + \frac{2}{3} - \frac{4}{3\sqrt{3}}\ln\frac{2+\sqrt{3}}{2-\sqrt{3}} \tag{3.11}$$

p0425   A step-by-step derivation is provided by Meyers et al. [107]. The most important parameter in Eq. (3.10) is the grain-boundary diffusion coefficient presented in the following equation [107] for stainless steel:

$$\delta D_{\mathrm{GB}} = 2.0 \times 10^{-16}\exp\left[\frac{-167\ \mathrm{kJ/mole}}{RT}\right](\mathrm{m}^3/\mathrm{s}) \tag{3.12}$$

p0430   For the grain rotation calculation, the grain-size diameter is taken as 200 nm. For $T = 800$, 900, 1000 and 1100 K, the plots are given in Figure 3.24B. The grain-boundary width, variously taken as $0.5-1$ nm, is not needed because it is embedded into Eq. (3.12). The rate of rotation decreases with increasing θ and asymptotically approaches $30°$. The temperature rise inside the band was not calculated in this study because of the uncertainty in the shear strain. Nevertheless, it has been done before [32], and the preceding values are within the range of values to be expected. Meyers et al. [32] estimated the temperature to be equal to ~ 800 K for a shear strain of 10 and equal to ~ 1000 K for a shear strain of 35 (Figure 3.19). Figure 3.24B shows that the rotation of a 200 nm grain from a rectangular to equi-axed takes place in 0.5 ms. This is on the order of the deformation time. Thus, it is feasible to assume that the equi-axed structure develops during deformation.

Dynamic Deformation/Adiabatic Shear-Band Formation

p0435 Figure 3.24B shows that for 1100 K, grain rotation of $30°$ takes place in 1.4 μs, whereas with decreasing temperature, it progressively takes a longer time. For example, for a rotation of $30°$, it takes 0.9 ms at 800 K compared with <1.4 μs at 1100 K. The calculations predict significant rotations of the boundary within the deformation time ($\sim 1-64$ μs) at temperatures between 900 and 1100 K for micro-grain sizes of $0.1-0.3$ μm. Thus, the reorientation of the grain boundaries can take place during plastic deformation. This does not exclude the possibility of reorientation/accommodation of the grain boundaries during cooling. The existence of both elongated and/or rectangular subgrains scattered in the centre of shear bands in 316 stainless steel [108], with a composition not too different from the alloy used in this study (12% Ni, 17% Cr), is strong evidence for the mechanism of equi-axed grain formation by the rotation of boundaries described previously.
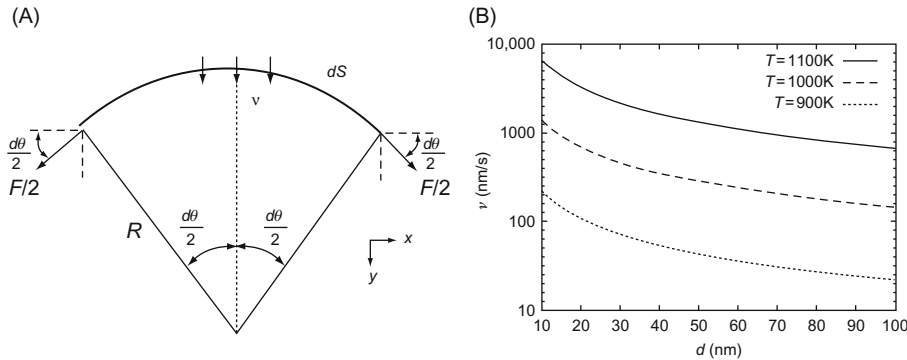
Grain-Boundary Mobility

p0440 The grain-boundary mobility can be calculated using the analysis developed by Rath and Hu [109]. The driving force on a grain boundary can be simply estimated by equating the force acting on a curved segment of dS due to the grain-boundary energy, γ. The total force acting on the grain boundary in the y direction (Figure 3.25A) is

$$F = 2\gamma \sin \frac{\mathrm{d}\theta}{2} \approx \gamma \mathrm{d}\theta \text{ (because } \theta \text{ is considered small)} \tag{3.13}$$

p0445   Therefore,

$$\text{force/area} = \frac{\gamma \, \mathrm{d}\theta}{R \, \mathrm{d}\theta} = \frac{\gamma}{R} \tag{3.14}$$

f0130   **Figure 3.25** (A) Schematic representation of a grain boundary with curvature $1/R$. (B) Calculated velocity of a grain-boundary migration from the Rath-Hu equation at three temperatures: 900, 1000 and 1100 K.

p0450   The velocity of the grain boundary is proportional to the force acting on the segment dS,

$$v \propto \frac{\gamma}{R} = M\frac{\gamma}{R} \tag{3.15}$$

where M, grain-boundary mobility, is the proportionality constant. The mobility is exponentially dependent on temperature through an Arrhenius-type relationship [109]:

$$M = M_0 \exp\left(\frac{-Q}{RT}\right) \tag{3.16}$$

p0455   For steel [110,111]: $Q = 140$ kJ/mol, $M_0 = 3.5 \times 10^{-7}$ m^4/J/s and $\gamma = 0.835$ J/m^2.

p0460   Assuming $d/2 = R$, where d is the grain size, grain-boundary velocity is plotted against grain size in Figure 3.25B for three different temperatures, 900, 1000 and 1100 K. For $d = 100$ nm (the lower limit of grain sizes observed in shear bands), $v = 22$ nm/s at 900 K. The plots at 1000 and 1100 K exhibit higher velocities: $v = 141$ and 652 nm/s, respectively. Thus, a grain-boundary movement of 22 nm at 900 K can be expected in 1 s. This cannot be sufficient to reorganize the deformation grain configuration. In contrast, for a shear band, the cooling takes place in time scales of fractions of milliseconds. For 1 ms and a grain size of 100 nm ($v = 0.01$ m/s), a displacement of 10 nm is obtained. Thus, this simple mobility calculation shows that no significant grain growth occurs on cooling and that recrystallization occurs by rotation of the boundary. Rath and Hu [109] use a   AU : 66

similar expression, except for the exponent, m, which depends on the grain-boundary misorientation and grain-boundary purity:

$$v = M\Delta F^m = M\left(\frac{\gamma}{R}\right)^m \tag{3.17}$$

p0465   In their experiments, m varies from 1 to 4. This can be attributed to grain-boundary solutes and misorientation.

s0080 *Kinetics of the Grain Growth*

p0470 Dynamic recrystallization is currently considered to be the nucleation and growth of new grains. They nucleate either homogeneously or heterogeneously along the elongated substructural boundaries of the deformed material. Li et al. [111,112] proposed that the growth of these new nuclei of the recrystallized grains should be related to both strain rate and atomic thermal migration. For the former case, the growth rate is associated with a strain, and it can be expressed by the following equation:

$$\dot{D}_2 = \frac{\alpha\mu b}{2\eta}D_2^2\sqrt{\frac{2\rho_m}{3}}\dot{\gamma} \quad \text{or} \quad \frac{dD_2}{d\gamma} = \frac{\alpha\mu b}{2\eta}D_2^2\sqrt{\frac{2\rho_m}{3}} \tag{3.18}$$

In Eq. (3.18), $D_2 = D_1\left(\frac{1}{1 - B(\gamma - \gamma_c)D_1}\right)$ is an average diameter of the recrystallized grains, where $B = \frac{\alpha\mu b}{2\eta}\sqrt{\frac{2\rho_m}{3}}$, γ_c is the critical strain stopping the subgrain rotation, η is the boundary energy density, D is the equivalent diameter of the cell structure (or subgrain), $\alpha\mu b^2$ is the energy per unit length of dislocation (α: a constant of $0.5-1.0$ [113]), δ is the cell wall width, ρ_m is the mobile dislocation density, γ is the strain and $\dot{\gamma}$ is the strain rate. On the other hand, formation of a shear band results in a temperature rise in the band, which also leads to the growth of recrystallized grains. The growth rate of the recrystallized grains has to be related to the atomic thermal migration, and it is expressed by:

$$\frac{dD_3}{dt} = (D_{B_0} + k_1\gamma D_B^V t)\left(\frac{2\eta}{D_3} + \frac{2\tau_i^2}{E}\right)\frac{\Omega}{\delta kT} \tag{3.19}$$

where $D_{B_0} = D_0'\exp(-Q_B/RT)$ and $D_B^V = D_0''\exp(-Q_B/RT)$, D_B^V is the vacancy diffusion coefficient in the grain boundary, D_{B_0} is a grain-boundary diffusion coefficient, $\Omega = b^3$ is the atomic volume, Q_B is the activation energy of the grain-boundary diffusion, D_0' and D_0'' are the pre-exponential factors, R is the gas constant and T is the absolute temperature.

p0475   The effects of both high-strain rate and the atomic thermal migration should be taken into account simultaneously while we discuss the nucleation and growth of

dynamically recrystallized grains. The former is an athermal process, and the latter is related to the thermal diffusion. Li et al. [111] superimposed these two effects and obtained the grain growth rate during localization in the bands, which is expressed as follows:

$$\frac{\mathrm{d}D}{\mathrm{d}t} = (D_{B_0} + k_1 \dot{\gamma} D_B^V t)\left(\frac{\eta}{D} + \frac{\tau_i^2}{E}\right)\frac{2\Omega}{\delta kT} + \frac{\alpha \mu b}{2\eta}D^2\sqrt{\frac{2\rho_m}{3}}\dot{\gamma} \qquad (3.20)$$

This equation can be solved by using a numerical method [112]. The calculation shows that the new grain diameter (D) increases almost linearly with time (t), and after several microseconds, it shifts to an exponential growth. However, according to the Gurney equation, the current test is over in 2.4 ms, so grain growth would be extremely low at this point, suggesting that any real growth is not really happening during the loading of the test and is occurring purely thermally post-mortem. This calculation essentially arrives at the same result as the one in Section 7.2. Li et al. [111,112] calculated the recrystallized grain size in a Ni−Cu−Al alloy, and the result (the grain size ~13−200 nm in diameter) is in reasonable agreement with TEM observations. This implies that the theoretical approach based on the kinetics of the recrystallized grains during dynamic deformation may be also valid in conditions of our test.

AU : 19

s0085 3.10 Deformation and Microstructure Within the Bands

### s0090 3.10.1 Super-High-Strain-Rate Deformation

p0480 It is known that once localized shear deformation has commenced, steep strain and strain rate as well as temperature rise will appear in the shear bands. Li [111] has calculated the deformation behaviour in the white band in α-Ti shown in Figure 3.26, where you can see that the grains were sheared for a relative movement; e.g. the displacements from a to a′, b to b′ and c to c′ occur during localization. From which, it is found that the width of the band is 12 μm, and the average shear strain measured is 5.2. According to the equation of Dodd and Bai [114], the half-width of the shear band is

$$\delta = \left(\frac{\lambda \theta_*}{\sigma_* \dot{\gamma}_*}\right)^{\frac{1}{2}} \qquad (3.21)$$

and the temperature rise in the band obtained by assuming that 90% of deformation work is converted into heat is

$$\theta_* = \frac{0.9 \tau_* \gamma_*}{\rho.c} \qquad (3.22)$$

f0135
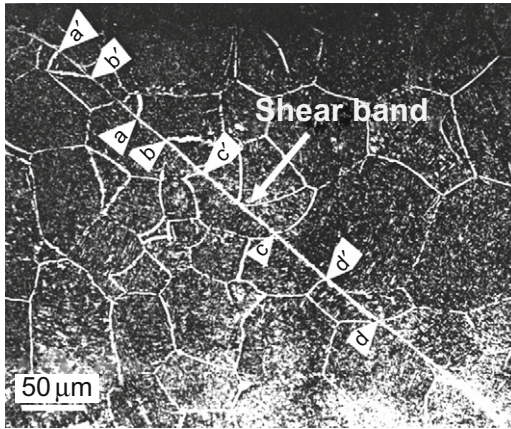
Figure 3.26 White shear band in α-Ti developed during dynamic compression [111].

p0485   The time required for shear-band formation can be obtained by the following equation, from Eqs (3.21) and (3.22):

$$t = \gamma_* / \dot{\gamma}_* = \frac{\rho c}{0.9 \lambda} \delta^2 \tag{3.23}$$

where $\tau_*, \dot{\gamma}_*$ are the shear stress and strain rate, θ_* is the temperature rise in the band, λ is the coefficient of the heat conduction, ρ is the material density and c is the heat capacity. The parameters used in Eq. (3.23) are $\rho = 4.5 \ g/cm^3$, $c = 0.473$ J/g K and $\lambda = 14.63$ W/m K for α-Ti. Therefore, $t = 0.1616\delta^2$, where the unit of the t is microsecond, and the unit of the δ is micrometre. From Eq. (3.23), it is found that the time required for formation of the band is 5.8 μs, and, therefore, the strain rate that the shear band underwent is $9 \times 10^5 \ s^{-1}$, which is higher by two orders of magnitude than the average strain rate $(2 \times 10^3 \ s^{-1})$ required for shear-band formation, implying that formation of the shear band may accompany an abrupt increase in strain rate. In other words, the materials within the band underwent a super high-strain-rate deformation. This is confirmed further in Al−Li alloy [56]. Xing et al. [115] developed a numerical model that simulated the evolution of the shear banding from several finite amplitude disturbances (FADs) in both temperature and strain rate and found that the shear banding process beyond plastic instability consists of two stages: inhomogeneous shearing and true shear banding. In the first stage, localized deformation occurs, and then localization is gradually restricted into a narrow band companying a burst enhanced in strain rate, and also both temperature and strain are raised as shown in Figure 3.27.

p0490   Giovanola [52] found that shear localization occurs in two sequential stages in VAR 4340 steel: during the first stage, the strain rate $(10^4 \ s^{-1})$ jumps by more than an order of magnitude to values larger than $10^5 \ s^{-1}$, then approaching
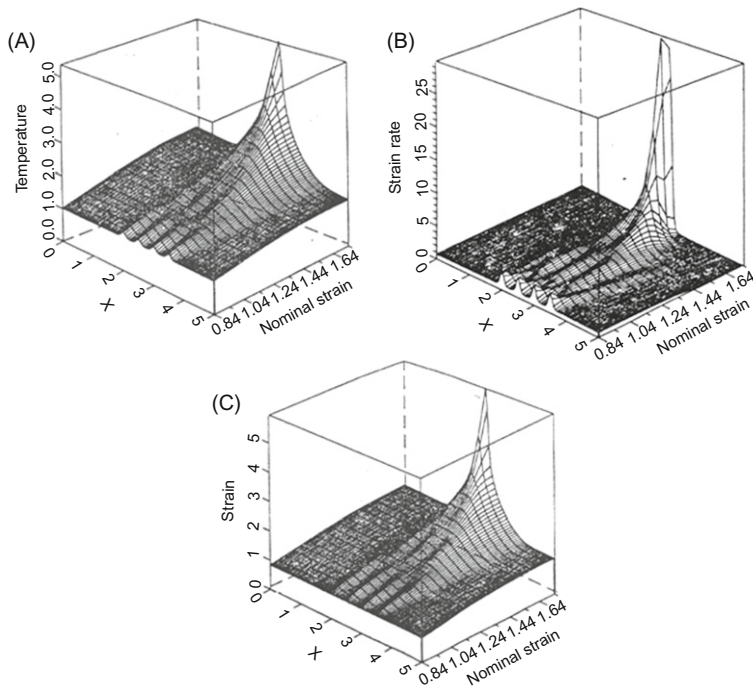
f0140   **Figure 3.27** Simulation of evolution of localized deformation: (A) temperature, (B) strain rate and (C) strain [115].

$1.4 \times 10^6 \, \text{s}^{-1}$ during second localization. The deformation behaviour with super high-strain rate in the band mentioned earlier was in good agreement with the numerical simulation [52,115].

p0495   A number of investigations show that a polycrystalline material with high-strain-rate sensitivity will appear to deform by a mode of super-plastic flow. First, the structures in the bands are very fine. Second, the temperature in the bands may reach and even exceed the melting temperature. These provide the conditions for super-plastic deformation of the materials. Ashby et al. [116] have proposed a con-stitutive equation to describe super-plastic flow of a material under high-strain rate. They suggested that when polycrystalline matter is deformed at temperatures above $0.4 \, T_\text{m}$ (the melting temperature), one possible mode of super-plastic flow is a 'diffusion-accommodated flow'. Dodd and Bai [114] have pointed out that, in the process of machining, although the average strain rate may be quite low, the strain rate in the bands of shear may be markedly higher. Murr et al. [117] have also sug-gested that the shearing deformation actually achieved inside an adiabatic band is extremely large, and the mechanism involves DRX and super-plastic flow. Indeed, it has been proposed that the extensive plastic deformation undergone by shaped

AU : 20

charges is connected to the nanocrystalline grain structure generated by the deformation of the liner [118].

s0095 ## 3.10.2   Formation of the Shear-Band Network

p0500 In some cases, you can find the large and complex networks of the shear bands. To understand the formation of the band networks, Li [111,112] has designed a special specimen with a shape of the conical frustum of Ti alloy deformed dynamically. He found that localized deformation occurred on the cone, and the region deformed was limited to a thin conical shell, so that different types of shear-band networks were observed on the longitudinal (Figure 3.28A) and transverse (Figure 3.28B) sections through the central axis. From these observations, he pointed out that the adiabatic shear bands were formed initially at the location of the maximum shear stress, and the actual deformation localization zone was confined in a conical shell in this kind of specimen with axial symmetry [118].

s0100 ## 3.10.3   Deformation Structures

p0505 It is generally accepted that the tendency is weakened for dislocation cross-slip and strengthened for the dislocation pile-up when the stacking fault energy decreases in FCC metals. Thus, the dislocations may extend into two partial dislocations, and AU : 21 there is a piece of stacking fault in between them. Figure 3.29 shows a shear band (Figure 3.29A) and its magnifications taken from the circle area (Figure 3.29B and C). It is characterized by twins and stacking faults as well as partial dislocations. Analysis shows that these dislocations are the partials with a Burgers vector of $\frac{1}{6}\left[\overline{1}\overline{1}2\right]$. In addition, it is found that the stacking faults may overlap each other during movement on the parallel slip planes, and the intrinsic and extrinsic stacking faults are separated by the partial dislocations [81].

p0510   The effect of shock on a microstructure is known and has been documented by Murr [119]. Lee et al. [120] have investigated the microstructure of the band in
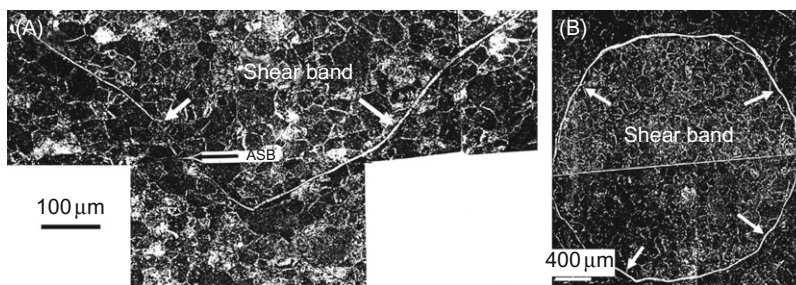
f0145 **Figure 3.28** Complex shear-band networks formed in Ti alloy subjected to impact compression by a split-Hopkinson bar: the shear-band networks observed on the longitudinal (A) and transverse (B) sections through the central axis [111,112].
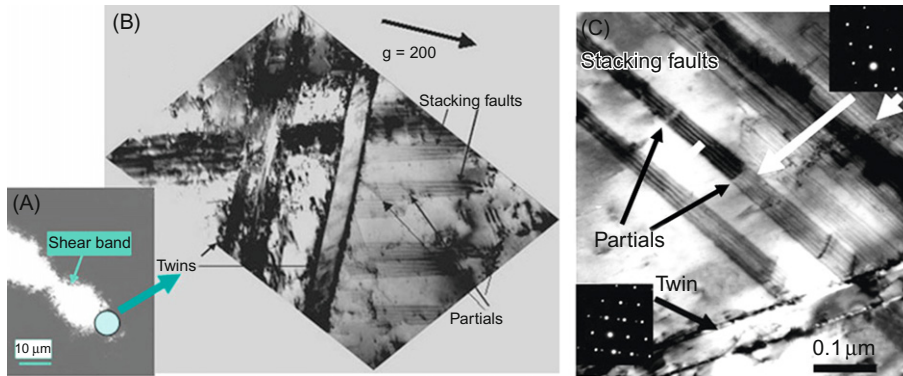
f0150   **Figure 3.29** TEM images of a shear band at (A) low magnification, and dislocation structures of the band taken from the circle area in the band are shown in (B and C) [77].
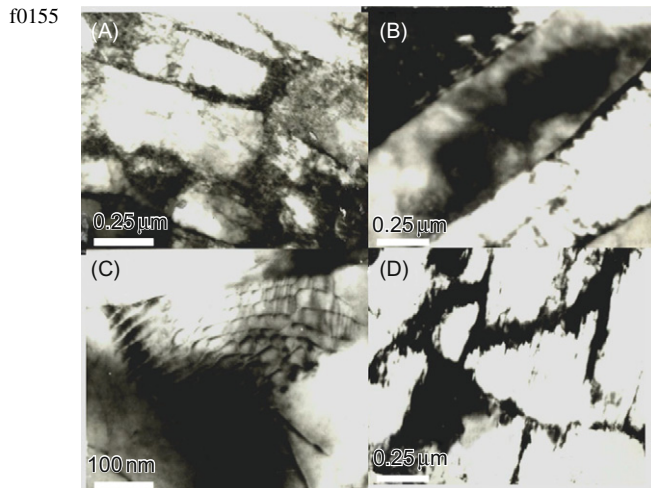
f0155

Figure 3.30 A set of the TEM images, showing the dislocation structure in the low-carbon steel subjected to dynamic torsional loading: elongated dislocation cells along the band and high dislocation density at the cell walls (A and B); dislocation network (C) and avalanche of the cells (D) [26].

HY-100 steel and found that the centre of the bands contains a mixture of the highly elongated subgrains and fine equi-axed cells with high dislocation density, and that the misorientations of 80% of random cells have the angles with less than about 5°. They proposed that the primary metallurgical process occurring in the bands is dynamic recovery, resulting in highly elongated subgrains as well as more equi-axed cellular structures. Meyers et al. [121] have found that the equi-axed cells are replaced by the elongated cells and that these elongated cells inside the band break down and are replaced by small grains with a relatively low dislocation density. Therefore, they attributed this kind of microstructure to dynamic recrystallization. Figure 3.30 is an image taken from a shear band in a low-carbon steel

f0160
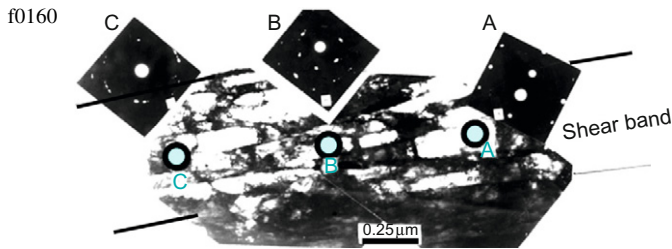
Figure 3.31 Microstructure within the shear band generated during dynamic loading in low-carbon steel [26].

with the structure of the ferrite−cementite [26]. Several feature characteristics are noteworthy. First, the α-ferrite in the band formed the tangled structure and the dislocation cells. The elongation and arrangement of the cells tend to be aligned along the shear direction, and the cell walls are full of dense dislocations as shown in Figure 3.30A. Second, the interfaces between the ferrite and cementite, as the sources, could release a great deal of dislocation (Figure 3.30B). Analysis indicates that the majority of dislocations are single dislocations with Burgers vector 1/2 [111] lying on a plane (1$\bar{1}$0) and 1/2[1$\bar{1}\bar{1}$] lying on a plane (110). These dislocations may interact with each other to form a stable network (Figure 3.30C) expressed by 1/2[111] + 1/2[1$\bar{1}\bar{1}$]→ [100]. It might be expected that the formation of the tangles, cells and networks of the dislocations could be responsible for the work hardening of the material during dynamic deformation. Third, the avalanche of the dislocation cells observed in the bands corresponds to the sharp drop of the load in the $\tau-\gamma$ response curve shown in Figure 3.30D. Fourth, the strain distribution is heterogeneous from place to place along the band. This can be seen clearly from the comparison of the SADPs from the different regions in the bands as shown in Figure 3.31. A relatively simple pattern obtained from the region A (marked by a circle) implies that the crystallographic nature of this area can be explained by slip deformation. On the other hand, however, in region C, it shows a spotty ring pattern, indicating the operation of multi-slip systems, arising from different subgrains with different suborientations. This examination reveals that the shear bands are highly localized deformation regions that may cross through many grains, implying that the shear bands may start on a governing slip system within one grain arising from the crystallographic slip, and then penetrate into adjacent grains by cooperative slip events that may involve a number of slip systems. This kind of cooperative slip may be assisted by both the stress concentration at the grain boundaries and the temperature rise in the band during localization.

AU : 22

p0515   Twinning is one of the basic plastic deformation modes in metals and alloys, in particular, under high-strain-rate loading. Figure 3.32 shows a structure composed of intersecting twins in a lightly deformed area outside the band in 304 stainless steel subjected to the cylindrical collapse (TWC) test with a strain rate of 10^4 s^{-1}. In Figure 3.32A, the thin foil orientation is close to [100], providing a perpendicular pattern of twins, which are on {111}. In Figure 3.32B, an incipient shear band is shown. The twins were distorted during localization. These twins have formed prior to the large deformation within the bands. They can be formed during the

f0165
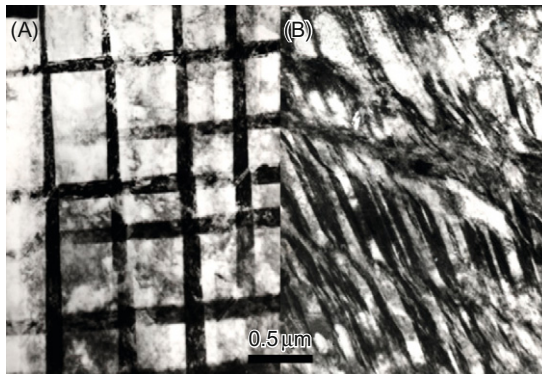
Figure 3.32 Primary twins inside (A) and the high-order twins outside the band (B) [32].
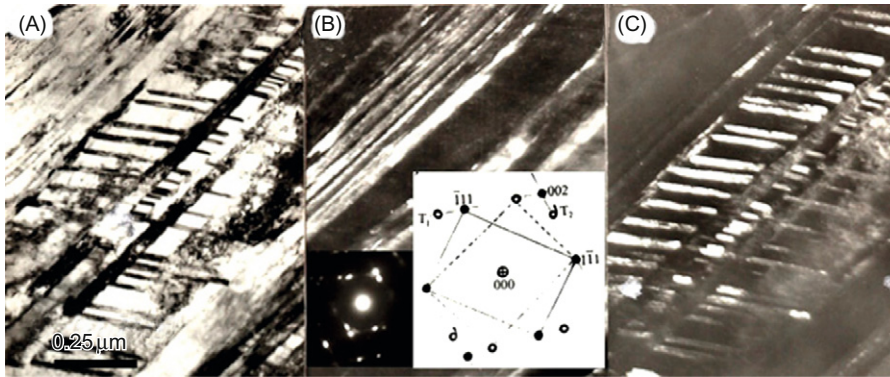
f0170 **Figure 3.33** (A) BF image of the twins; (B) and (C) DF images of the first-order twins and second-order twins and corresponding diffraction patterns and its index (insert): the representative from the matrix, first- and second-order twins, respectively [32].

AU : 63

passage of the first shock pulse, which precedes the implosion of the cylinder. Figure 3.33A shows the twins in greater detail. In addition to the first-order twins with a spacing of $0.1-0.2\,\mu m$, there are second-order twins with a much lower spacing (Figure 3.33C). The second-order twins imaged by HREM are shown in Figure 3.34. The atomic planes (111) and their change in orientation inside the twins are clear. These two-set twins are shown with a thickness of 20 nm each. A more detailed example is shown in Figure 3.35, displaying twinning and multi-order twinning structures within the bands produced in Ti−6Al−4V alloy subjected to explosive collapsed loading [81]. Figure 3.35A is a bright-field image, and Figure 3.35B and C shows dark-field image with spots T_1 and T_2 (insert), respectively. All of these results indicate that twinning is a favoured dynamic and continuously proliferated process for a material under high-strain-rate loading.
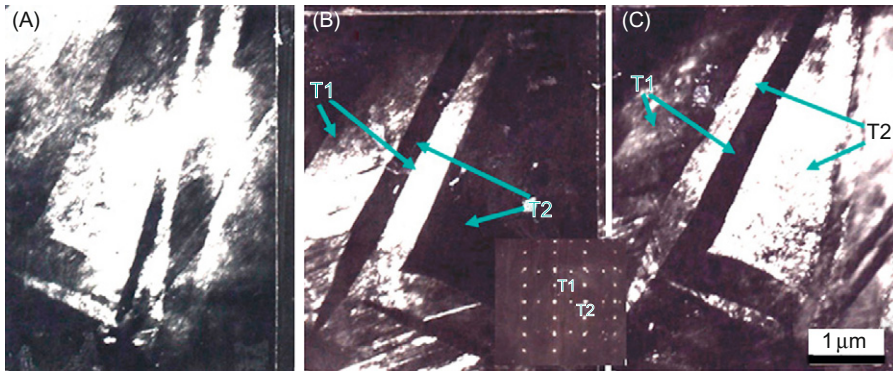
AU : 23

f0175
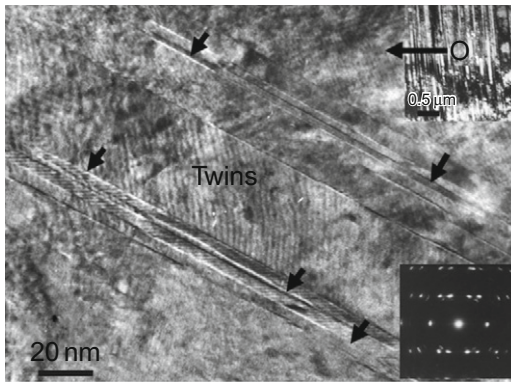
Figure 3.34 Multi-order deformation twins imaged by HREM [32].


f0180 **Figure 3.35** Multi-order deformation twins produced during explosive collapse of a TWC in Ti−6Al−4V alloy [81].

s0105 ### 3.10.4 Damage and Fracture

p0520 The interrupted tests show that the sudden drop appearing in the $\tau-\gamma$ curve, leading to the fracture, is caused by initiation and coalescence of the micro-cracks along the bands, rather than the formation of the shear bands [25,26]. The localized shear deformation may promote further the nucleation, growth and coalescence of the micro-cracks, and therefore accelerate the fracture of material along the bands. The degree of the structural damage in the shear bands, leading to final failure, can be assessed by SEM as shown in Figure 3.36. The number of cracks per square millimetre, which is an indication of the degree of the structural damage, was determined as a function of the distance from the boundary between the shear bands and matrix to the centre of the band of the dual-phase (DP) steel subjected to dynamic torsional loading. It can be seen that the nearer the centre of the band, the bigger the structural damage extent [34]. This is verified by the result of Al−Li alloy [56]

f0185
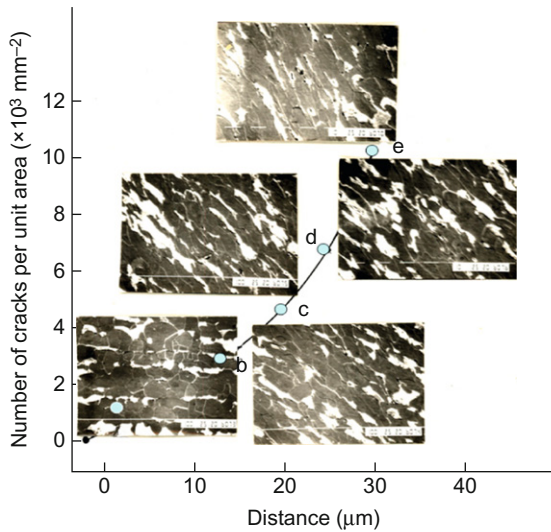
Figure 3.36 The relationship between the number of the cracks per square millimetre and the distance from the boundary of the band to the matrix in the shear band in low-carbon steel [34].
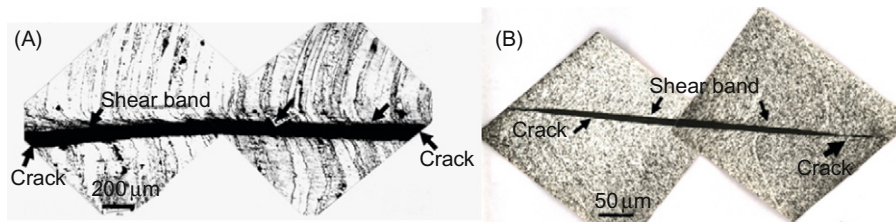

f0190 **Figure 3.37** Fracturing along the shear bands in Al−Li alloy [56] (A) and SiC/Al composite (B) [90].

(Figure 3.37A) and Al/SiC composite [90] (Figure 3.37B), where the final break is obvious along the shear band. The fracture of a material subjected to dynamic loading was classified into both ductile and brittle natures [14,18,122]. Rogers has reported [14] that if the fracture is ductile, it almost certainly occurred during adiabatic deformation when the band was hot and weak. On the other hand, brittle fracture occurs subsequently to the termination of deformation and the quenching of the hot band by the adiabatic matrix material to form the hard, brittle, transformed structure. However, a number of observations of the fracture surface reveal that whether the fracture is along deformed-type bands in quenched martensite steels [26] or the white shear bands in Ti-55 alloys [63], their fracture topographies appeared to be of ductile characterized by the shear dimples on the fracture surface. The materials in the bands subjected to a large accumulated strain under high-strain rate, resulting in an abrupt temperature rise, seem to suffer an annealed or tempered treatment. Therefore, the fracture morphology in the quenched steel deformed at high-strain rate appears to be similar to those in the annealed or tempered steels, and thus it is reasonable to propose that in addition to the stress-state condition, the temperature

rise within the band plays an important role in failure of materials along the bands [14,26]. The temperature rise in the band is so high that it can cause recrystallization or even melting, leading to softening of material in comparison with that in the adjacent matrix. Timothy et al. [23] assumed that the void formation in adiabatic shear bands in titanium alloys was intimately associated with thermal softening and local melting of the metal in the bands. This is the reason that, in all cases, the fracture surface topography observed is entirely of a ductile nature, irrespective of whether it is occurring in the deformed or white etching bands in quenched and tempered steels. Figure 3.38A shows voids that nucleated and grew inside the shear band in a Ti−6Al−4V alloy [31,81]. If, subsequent to void nucleation, there is a combined action under tension and shear stresses, these voids grow until their edges reach the boundary of the shear band. Then they do not grow into the surrounding material because of its higher yield strength. The voids became gradually ellipsoidal, as they elongate along the shear bands. This sequence is shown in Figure 3.38B. As they grow, they eventually coalesce, forming a crack. Zhou et al. [70] measured the velocity of propagation of the shear bands in a Ti−6Al−4V alloy impacted at a velocity of 50 m/s. Their propagation velocities were 50−5 m/s. Xue et al. [123] used the TWC method, which had an initial wall velocity of 200 m/s and obtained a propagation velocity of 556 m/s, inferred from their experimental results. This great difference can be explained through Mercier and Molinari's analysis [124]: the imposed velocity C determines the shear-band velocity V through the equation

$$V = \frac{\sigma_\mathrm{f}}{\rho C} g\left(\frac{\lambda}{h}\frac{t}{h}\right) \tag{3.24}$$
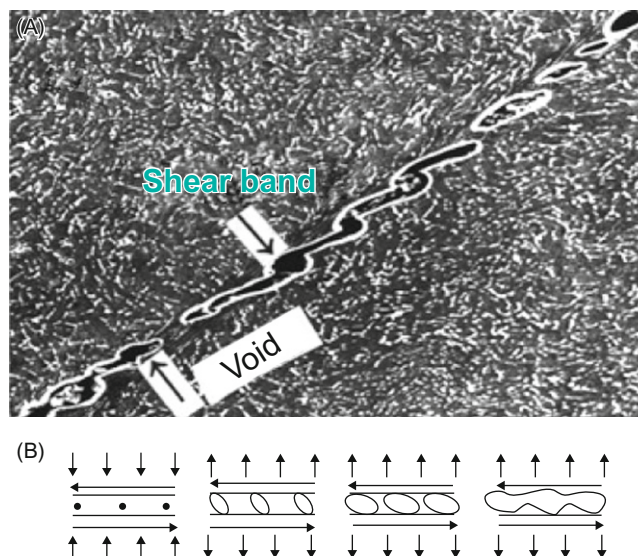
f0195 **Figure 3.38** Initiation and coalescence inside bands (A) and schematic representation of sequence of events leading to ductile failure (B) [31,81].

f0200
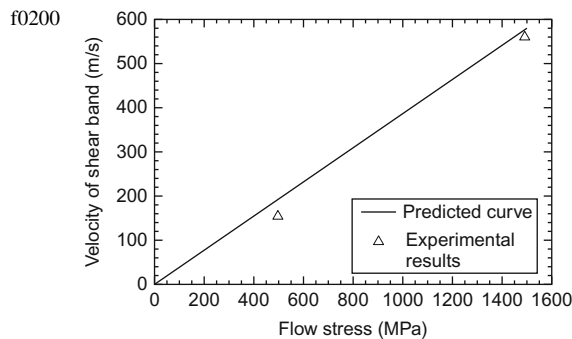
Figure 3.39 Shear-band velocity as a function of flow stress for Ti alloy; comparison of Mercier−Molinari's theory [124] with results by Xue et al. [31].

where σ_f is the material flow stress, and g is a function of λ/h, the normalized process zone length, and t/h, the normalized shear-band thickness. The effect of flow stress on the velocity of propagation of the shear band is shown in Figure 3.39. Two experimental points are given: one for Ti and one for Ti−6Al−4V, with a flow stress approximately triple the one for pure Ti. There is a linear relationship between flow stress and V, for the same external conditions, and g. The experimental results by Xue et al. [123] compare well with the Mercier−Molinari predictions.

s0110
3.11 Spacing and Self-Organization of the Shear Bands [31,125]

p0525 Most of the current theories on prediction of spacing of shear bands are based on the analysis of a single shear band along its propagating direction.

p0530 We briefly describe the evolution of multiple adiabatic shear bands in commercially pure titanium and Ti−6Al−4V alloy through the radial collapse technique of a TWC under high-strain-rate deformation. Shear-band initiation, propagation and spatial distribution were examined under increasing global strains. As an illustration, Figure 3.40A shows the pattern of helicoidally shear bands in a Ti−6Al−4V specimen, whereas Figure 3.40B shows the size and spatial distribution of shear bands at a global effective strain of 0.264. The shear bands nucleate at the internal boundary of the specimens and construct a periodical distribution at an early stage. The shear bands undergo bifurcation as they progress in their spiral trajectory and as their spacing increases. The shear bands are favoured initiation sites for failure, which occurs by void nucleation and growth, and then coalescence inside the thermally softening regions. The evolution of the morphology of the voids is determined by the restrictions imposed by the bands. Figure 3.41 shows that the shear-band spacing is quite dependent on the material, being much lower in 304 stainless steel than in Ti−6Al−4V. The differences of mechanical response between the two alloys are responsible for significant differences in the evolution of the shear-band patterns. The same differences are observed between titanium and Ti−6Al−4V. Figure 3.42 shows how the shear-band spacing and its evolution determine the fragmentation of a cylindrical specimen. The number of shear bands
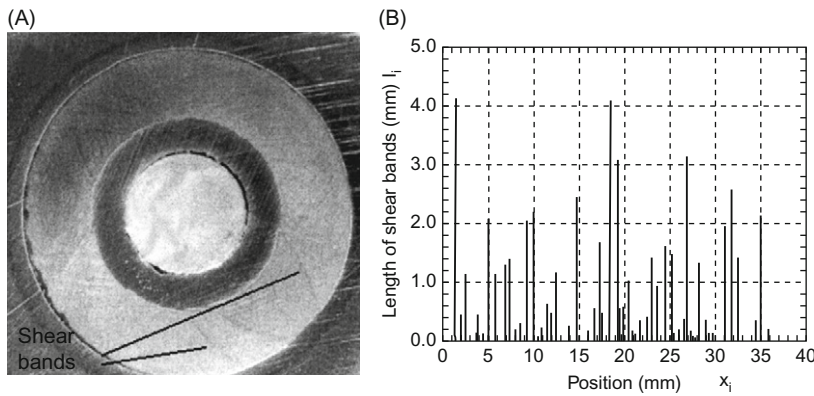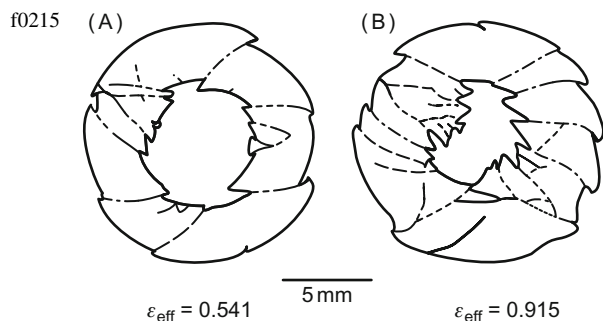
f0205 **Figure 3.40** Shear-band pattern of Ti−6Al−4V alloy at well-developed stage $\varepsilon_{eff} = 0.254$: (A) shear-band pattern and (B) spatial distribution [31].
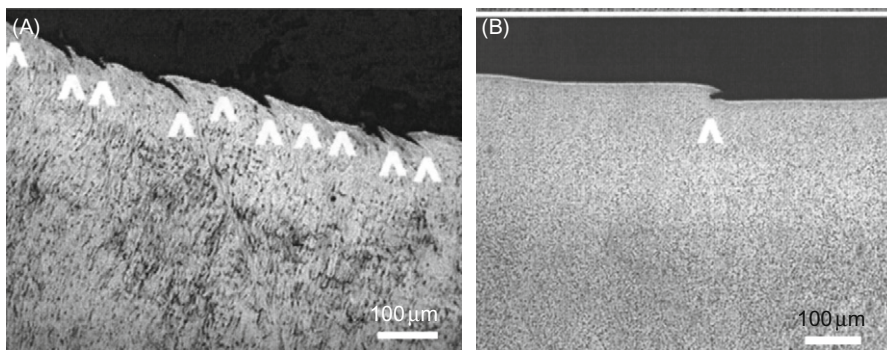
f0210 **Figure 3.41** Comparison of spacing for stainless steel (A) and Ti−6Al−4V alloy (B) at initial stage [31].

initiated in Ti (spacing of 0.18 mm) is considerably larger than in Ti−6Al−4V (spacing of 0.53 mm). The experimentally obtained shear-band spacings are compared with theoretical predictions [39,41,42] in Table 3.4. The shear-band interactions are more complex than previously thought, and their spacing cannot be predicted by the one-dimensional perturbation theories [41,42]. The Grady−Kipp theory cannot accommodate the increased spacing as the shear-band size increases because it is also one-dimensional. This was done by Xue et al. [31,125]. Thus, the treatment needs to incorporate the following elements:
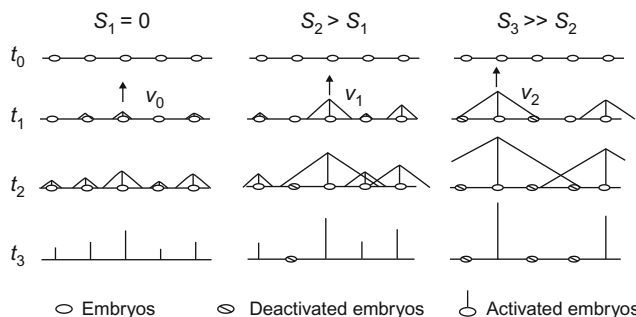
u0070 • *Rate of nucleation of shear bands*: The probability of nucleation, $p(v_o, s_o)$, in a reference volume v_o, or surface s_o, was successfully described by a Weibull distribution in which the stress was replaced by strain as the independent variable. Parameters defining the distribution are a critical strain for nucleation, a mean nucleation strain and a Weibull

f0215

(A)   (B)

$\varepsilon_{eff} = 0.541$ 5 mm $\varepsilon_{eff} = 0.915$

Figure 3.42 Evolution of the shear-band pattern in Ti−6Al−4V alloy [31].

**Table 3.4** Prediction and Experimental Results for Stainless Steel and Titanium

Spacing (mm)	Experimental Data Initial Level	Experimental Data Developed	L_{WO} (mm)	L_{GK} (mm)	L_{MO} (mm)
SS 304L	0.12	3.2	0.17	2.62	0.16
CP Titanium	0.69	2.57	0.52	3.3	0.36

$S_1 = 0$ $S_2 > S_1$ $S_3 >> S_2$

t_0

t_1 v_0 v_1 v_2

t_2

t_3

○ Embryos   ◔ Deactivated embryos   ⌇ Activated embryos

f0220 **Figure 3.43** Two-dimensional representation of concurrent nucleation and shielding. S is a shielding parameter; as S increases, the release of stress produced by growing shear bands deactivates embryos. For $S = 0$, all embryos are activated, and shear-band spacing is small. For a large value of shielding S_3 (right side), only a fraction of embryos are activated.

modulus. There can also be shielding at the nucleation stage, depending on the relative values of the rate of nucleation and rate of growth.

u0075 • *Rate of growth or velocity of propagation*: This is an important factor in their self-organization. Shear bands compete among themselves and gradually change their patterns. A 'Darwinian' natural selection takes place, and a large number of small bands evolve gradually into a smaller number of large bands, due to the shielding of stresses produced during growth. Such evolution of shear-band pattern occurs under a homogeneously distributed pressure acting on the external boundary of the cylindrical specimen. This is a typical self-organization. This is schematically rendered in Figures 3.43 and 3.44.
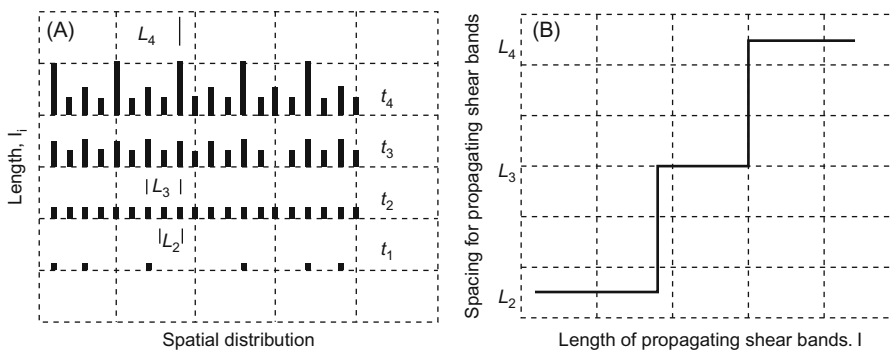
Figure 3.44 (A) Schematic diagram of the evolution of shear-band spacing at different levels. t_1, random initiation; t_2, self-organization into 'periodic' pattern among nuclei; t_3, some shear bands grow faster suppressing others; t_4, self-organization of developed shear bands. (B) Spacing of propagating shear bands as a function of length.

p0545   This theory was developed by Xue et al. [31,125] and applied to Ti, Ti−6Al−4V and 304SS. It clearly needs additional work.

s0115 3.12 Effect of Dynamic Strain Aging

p0550 Many alloys (steels, titanium and aluminium alloys) that undergo dynamic strain aging are also prone to shear localization. What is the effect of the changes in thermal softening and strain-rate sensitivity on the development of shear bands?

p0555   Dynamic strain aging is a phenomenon that has its origin in the interaction of mobile dislocations with solute atoms. Cottrell [126,127] proved that solute atoms could form atmospheres around moving dislocations and retard their motion. He proposed that the minimum strain rate at which serrated flow initiates is

$$\dot{\varepsilon} = C \exp\left(\frac{-Q}{kT}\right) \approx 10^9 \, D \qquad (3.25)$$

where Q is the activation energy for diffusion, C is a frequency factor and D is the diffusion coefficient. The unit of D is cm^2/s.

p0560   The trapping of mobile dislocations by solute atoms produces a range of mechanical effects: serrations in the stress−strain curve (Portevin−Le Chatelier effect [128,129]), increased work-hardening rate, decreased ductility (the blue brittleness of steels) and a change in thermal softening, which leads, in extreme cases, to thermal hardening.

p0565   Dynamic strain aging has been observed in a number of alloys: steels [130,131], aluminium alloys [132], Ni−C alloys [133,134] and titanium alloys [135].

p0570   The literature abounds with dynamic strain aging measurements. The calculations are carried out herein for a low-carbon steel. The experimental results by
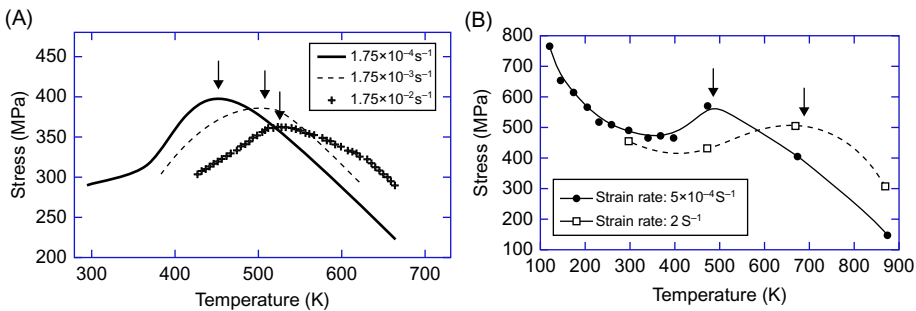
f0230 **Figure 3.45** (A) Effect of temperature on flow stress (5% plastic strain) of AISI 1008 steel [130] and (B) effect of temperature on flow stress of AISI 1020 steel [129].

Bergstrom and Roberts [136] (0.035 wt%C), Li and Leslie [137] (AISI 1008, 1020, 1035) and Gilat and Wu [134] (AISI 1020) serve as a basis for establishing the experimental parameters for DSA. Figure 3.45A shows the flow stress (at 5% plastic strain) for AISI 1008 steel [137] as a function of temperature at strain rates of 1.75×10^{-4}, 1.75×10^{-3} and 1.75×10^{-2} s^{-1}. Two effects are seen: (a) the flow stress increases with temperature in the region of $350-500$ K and (b) the peak temperature increases with the strain rate. Similar results are reported by Gilat and Wu (Figure 3.45B). The same effect is observed: a shift in the hump to higher temperatures as the strain rate is increased. The experiments carried out by Gilat and Wu [138] extend to a much higher strain rate, and the hump is at 720 K for a strain rate of 2 s^{-1}. It is also known that the temperature for the hump is dependent on the strain rate but independent of the carbon content. The carbon content was varied from 0.035% [136] to 0.2% [138].

p0575   There are two effects that will modify the susceptibility to shear-band formation under these conditions:

o0010 **1.** The thermal softening decreases, with actually thermal hardening. This will oppose the formation of shear bands. However, this is followed by an accelerated softening on the right side of the hump.

o0015 **2.** The strain-rate sensitivity becomes negative in a special region. This will produce and enhance susceptibility to shear localization.

p0590   The exact nature of this interaction needs to be better understood, but it can be stated that if thermal softening is increased and the strain-rate sensitivity is decreased (or even negative), the tendency for shear localization is enhanced. This area needs additional research.

s0120 ## 3.13 Shear Bands in Nanocrystalline Metals and Metallic Glasses

p0595 The formation of shear bands in nanocrystalline, ultrafine-grained and glassy metals (especially, BMGs) is discussed here. These materials are characterized by
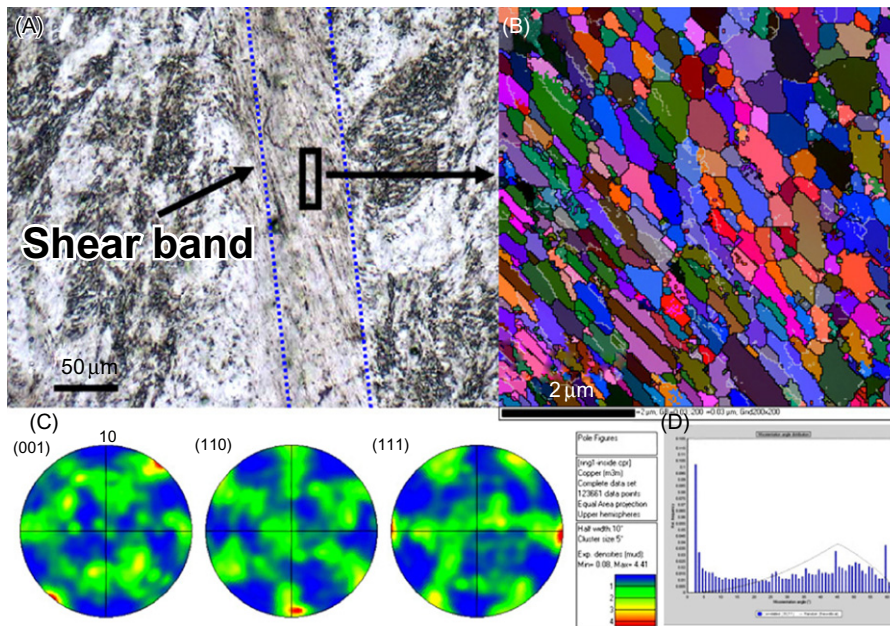
f0235   **Figure 3.46** (A) SEM showing shear band with width $\sim 50\ \mu m$, (B) EBSD image showing equi-axed and elongated recrystallized grains, (C) the pole figure and (D) the grain-size distribution.

low work hardening and are prone to shear localization, even when the external rate of load application is low.

p0600   Ultrafine-grained copper was subjected to the hat-shaped experiments, and forced bands were produced by Mishra et al. [139]. On close examination, the structure of these bands was quite different from that of the starting material, which has a grain size of $\sim 200-400$ nm. Figure 3.46 shows the width of the band, $\sim 50\ \mu m$, and its structure as revealed by SEM−EBSD. The material in the band clearly underwent recrystallization, and the grains grew to a diameter much larger than the original ones. In contrast, forced bands obtained earlier in copper were much larger. Shock-hardened copper had bands of $\sim 200\ \mu m$.

p0605   The grains in the band are both elongated with an average long/short axis ratio of about 2 (Figure 3.46B) and equi-axed with an average size of ~ 500 nm in diameter. Most grains have high-angle boundaries of $15-60°$ (Figure 3.46D), and there is no evident texture with a maximum of pole density of about ~ 5.2 (Figure 3.46C) [140]. These observations confirm further the previous proposal mentioned in Section 3.9 concerning the static/dynamic recrystallization mechanism operated in Fe−Cr−Ni monocrystals produced under high strain and high-strain rate.

p0610   The Bai−Dodd equation (Eq. (3.21)) was applied to predict the thicknesses. The results, shown in Figure 3.47, are quite different. There is a large drop for the

f0240
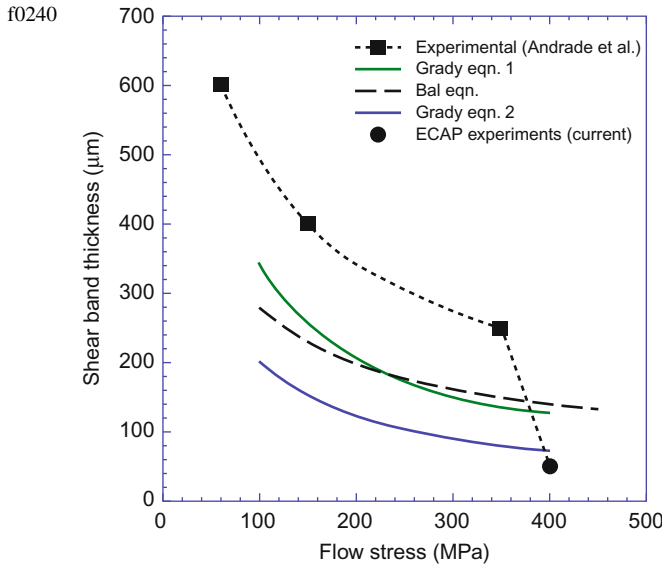
Figure 3.47 Shear-band thickness obtained from experiments as compared to prediction by Bai's and Grady's [141,142] equations. *Source*: From Ref. [139].

UFG copper. One of the reasons for this difference is thought to be the highly   AU : 24
unstable grain structure that undergoes softening at a higher rate than the others.
The Bai equation does not contain a thermal softening term. Grady [141] proposed
an equation that does. It is the term α in

$$\delta = \left(\frac{9\rho^3 C_p^2 \lambda^3}{\tau^3 \alpha^2 \dot{\gamma}}\right)^{1/4} \tag{3.26}$$

where λ is the thermal conductivity, and T, τ and $\dot{\gamma}$ are the temperature, stress and
strain rate, respectively, inside the band. The thermal softening rate, α, assumes lin-
ear behaviour:

$$\tau = \tau_0(1 - \alpha T) \tag{3.27}$$

p0615   Grady [142] later proposed another equation, where the term 9 is replaced by
16. Figure 3.45 shows the prediction from these equations and the as-measured
shear-band thickness from Cu experiments. Wright [59] states that the agreement
of Bai's equation with experimental results is usually within a factor of 2. For the
experiments carried out by Andrade et al. [143], there is a reasonable correspon-
dence with both Bai's [44] and Grady's [141] equations. The trend of the experi-
mental data parallels the two equations. Although both Bai's and Grady's equations
predict a decrease in band thickness with increasing flow stress, the precipitous
drop for the UFG copper has to be attributed to an additional mechanism for the

loss of mechanical stability. This can be due to the increased propensity of thermal softening in equal channel angular pressing (ECAP) samples. In the original formulation of Grady [141], this parameter assumes a linear thermal softening with the melting point marking the zero strength value. To simulate a more drastic thermal softening of the UFG copper, consistent with the microstructural instability, it is assumed that the full softening is achieved at 400 K. The results are plotted as Eq. (2) in Figure 3.47. Thus, the agreement with the Grady equation for the UFG specimen can be significantly improved by modifying the linear softening parameter, α.

AU : 25

p0620   The process of dynamic plastic deformation (DPD) pioneered by Lu and co-workers produces grain sizes significantly below those reached in either ECAP or high-pressure torsion (HPT). The deformation process is applied at 77 K and at a high-strain rate, on the order of 10^2 s^{-1}. This increases the Zener$-$Hollomon (Z$-$H) parameter of the process and consequently decreases the resulting grain size because the recrystallized grain size is found to correlate well with the Z$-$H parameter as it incorporates both temperature and strain rate:

$$\ln Z = \frac{1}{T} \ln \dot{\gamma} \tag{3.28}$$

p0625   These experiments were first conducted in pure copper by Li et al. [144] and then in copper$-$aluminium alloys by Hon et al. [145]. Plastic deformation in this regime produced a profusion of twins in addition to the ultrafine-grained structure. A third component of microstructural refinement set in at higher strains because of the lower temperature and higher strain rate: adiabatic shear-band formation. These are shown for Cu (Figure 3.48) and Cu$-$Al (Figure 3.49). The grain sizes are significantly lower than those obtained by Andrade ($\sim 200-400$ nm), by virtue of the higher Z$-$H parameter. An increasing tendency of deformation twinning and shear
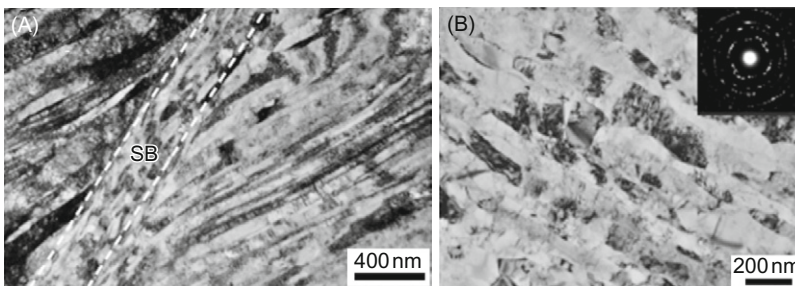
f0245   **Figure 3.48** Shear band (A) produced in structure consisting of nanosized twins (B) generated by successively deforming copper at LN temperature dynamically (10^2 s^{-1}); the process is called DPD.
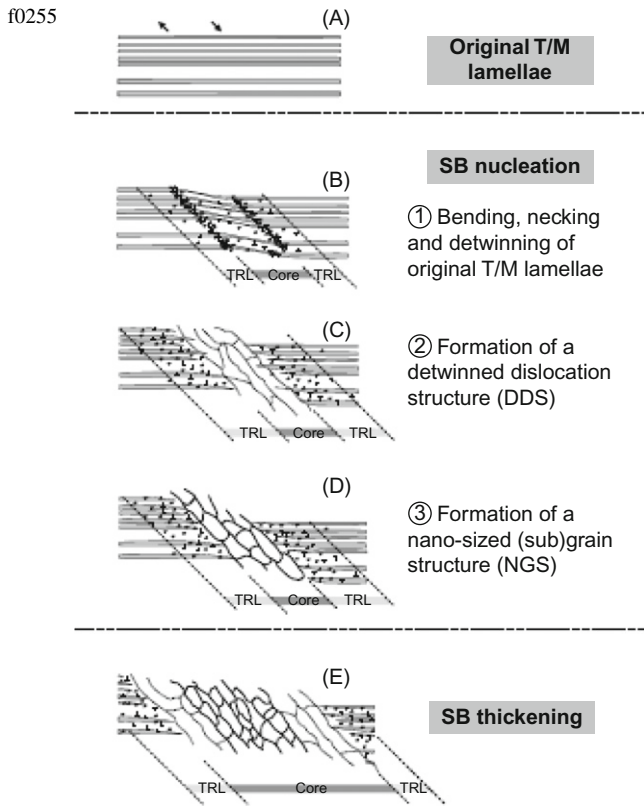*Source*: From Ref. [144].
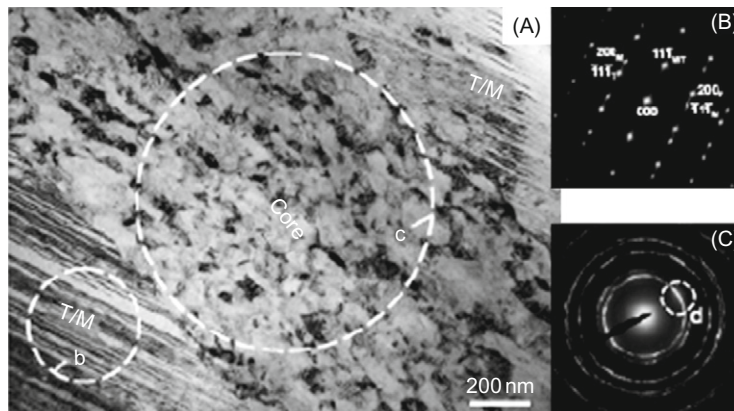
f0250   **Figure 3.49** Shear band in a Cu−Al alloy subjected to DPD at 77 K; the shear band traverses a nanoscale structure characterized by twins with a spacing of 20 nm; grain size in shear band is ∼60 nm. Diffraction patterns of (B) twinned region and (C) shear band. *Source*: From Ref. [141], Figure 3.12.

banding was observed at higher strains. For strain $e = 2.1$, a mixed nanostructure is formed in the DPD Cu bulk sample with nanoscale T/M lamellae making up about 33% of the volume, and nanosized grains making up about 67%. The nanograins can be classified into three types in terms of their origin: (a) nanograins derived from fragmentation of nanoscale T/M lamellae with an average transverse size of about 47 nm; (b) nanograins in shear bands with an average transverse size of about 75 nm; and (c) nanograins derived from dislocation cells with an average transverse size of about 121 nm. For Cu−Al the grain sizes are even lower, and these are indeed truly nanocrystalline structures. The mechanism by which a shear band forms according to Hong et al. [145], dissolving away the twin lamellar structure, is shown in the schematic sequence of Figure 3.50.

p0630   Metallic glasses deform primarily by the initiation and propagation of shear bands. The evolution of metallic glasses into BMGs enhanced the interest in these materials in a most significant manner. This was a development that owes a great deal to Johnson and co-workers [146,147] and more recently to Inouie [148]. Shear localization is observed frequently under both quasi-static and dynamic loading. The total uniform strain by BMGs is rather small. The release of the elastic energy stored in the system is the driving energy. There are two views on the softening mechanism leading to localization: thermal softening, observed by Lewandowski and Greer [149], and free-volume coalescence softening, proposed by Spaepen [150]. Dai et al. [151−153] performed experiments and calculations that indicate that both mechanisms are operative in the $Zr_{41.2}Ti_{13.8}Cu_{12.5}Be_{22.5}$ BMG.

p0635   Wright et al. [154,155] observed that the shear bands in metallic glasses loaded quasi-statically propagate a certain distance and then stop. This was accompanied by significant load drops. Some of these are shown in Figure 3.51.

f0255

Figure 3.50 Sequence proposed by Hon et al. [141] for the formation of shear bands in nanotwinned Cu−Al alloy.

f0260
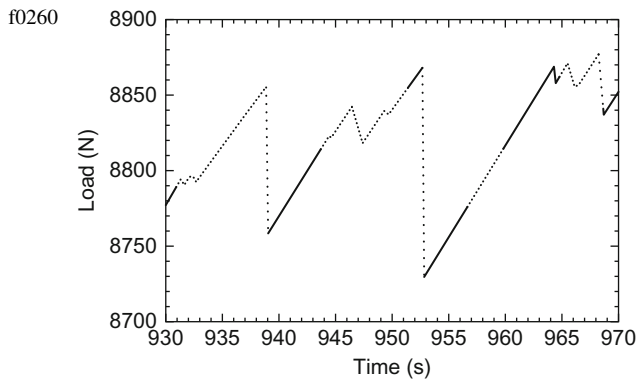
**Figure 3.51** Load drops associated with shear-band formation in Pd40Ni40P20. *Source*: From Ref. [154].

They observed the failure surface, and there was a clear evidence for melting, from spheroidal droplets. They calculated the temperature rise but concluded that it was low and could only reach significant levels during fracture. However, there are parameters in the calculations that are not well known, and assuming a rapid

f0265
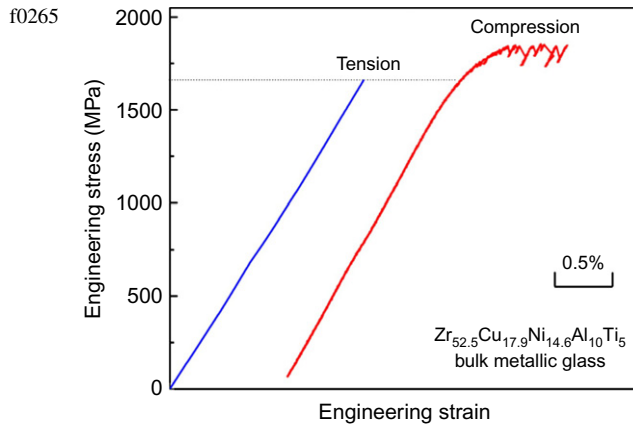
Figure 3.52 Engineering stress−strain curves of $Zr_{52.5}Cu_{17.9}Ni_{14.6}Al_{10}Ti_5$ (at.%) BMG in tension and compression; difference in strength ∼ 15%. Notice load drops in the compression curve. *Source*: From Ref. [156].
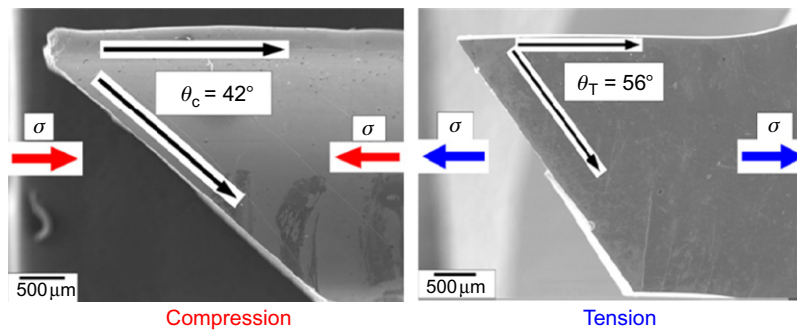

f0270   **Figure 3.53** Typical shear fracture modes of Zr-based BMG [$Zr_{52.5}Cu_{17.9}Ni_{14.6}Al_{10}Ti_5$ (at.%)].

propagation of the shear band under adiabatic conditions, significantly larger values are possible. Unknowns are the thickness of the shear band and the velocity of propagation.

p0640   Experiments by Zhang and co-workers [156,157] show that there is little difference between the compressive and tensile strength of BMGs. Two typical curves are shown in Figure 3.52 for $Zr_{52.5}Cu_{17.9}Ni_{14.6}Al_{10}Ti_5$. The compressive strength is slightly (∼15%) higher than the tensile strength. Load drops can be seen in compression testing, of the same nature as the ones observed by Wright et al. [154,155]. The failure in both tension and compression occurs by shearing, as demonstrated by the fractured specimens shown in Figure 3.53. The deviation in the angles from 45° was explained by Zhang et al. [158] in terms of a new failure criterion, modified from Mohr−Coulomb.

p0645   We suggest here that a possible explanation for the differences between the compressive and tensile responses can be due to thermal effects in the shear band. Figure 3.54 shows a sequence of events for a possible scenario in compression
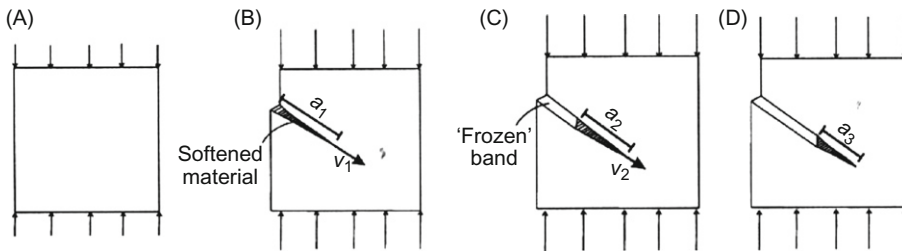
f0275   **Figure 3.54** Schematic sequence showing how a shear band initiates, propagates and arrests in a metallic glass subjected to quasi-static compression.
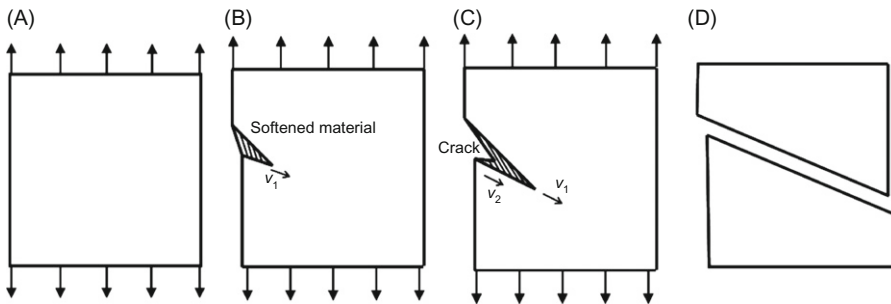

f0280   **Figure 3.55** Schematic sequence showing how a shear band initiates in tension and how a crack propagates along the softened path eventually overcoming band and fracturing BMG.

testing. A shear band initiates at the surface of the specimen (Figure 3.54B) and propagates at a velocity V_1. The thermally softened region has a length a_1. As the band propagates down (Figure 3.54C), the region away from the band cools down and can 'freeze' back. This reduces the driving energy for the band and reduces the length of the softened region to a_2. Thus, you would expect an associated reduction in propagation velocity to V_2. This velocity is reduced to zero in Figure 3.54D, when the softened region length reaches a critical size a_3. Each formation and arrest event leads to a load drop. Thus, the BMG exhibits a limited ductility in compression, propitiated by the successive formation and 'freezing' of shear bands.

p0650   On tensile deformation, the situation is different. After a shear band forms, softening the material, a crack can easily initiate at the surface and follow the advance of the shear band. In this scenario, shown by the sequence of Figure 3.54, the specimen fractures after the first band is initiated and propagated.

p0655   The scenarios presented in Figures 3.54 and 3.55 require thermal softening inside the band and support the hypothesis of thermal softening as an important drive for shear localization. The TEM results by Jiang and Atzmon [159] on Al90Fe5Gd5 are intriguing. They observed nanocrystallization in both the shear

f0285
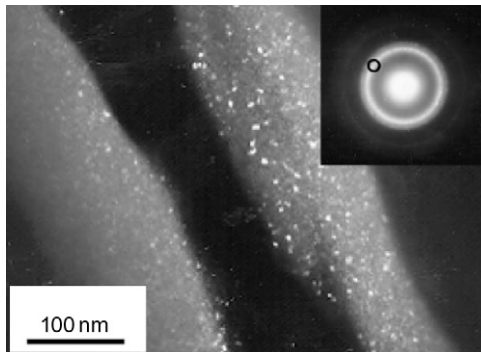
Figure 3.56 Nanocrystallization in shear band formed in compression deformation of Al90Fe5Gd5 BMG [153].

band and fracture surface. They attributed the precipitation of nanocrystallites in the compressive region in the shear bands to a kinetic effect due to the uniformly distributed free volume and the formation of the nanocrystallites at the fracture surfaces to adiabatic heating induced by fracture. The nanocrystals, having a few nanometres size and evenly distributed inside the shear band, formed in compression are shown in Figure 3.56.

p0660   It should be emphasized that different mechanisms operate under different conditions in different BMGs. Hence, the occurrence of thermal softening in no manner diminishes the importance of free-volume softening, which might dominate under specific conditions.

p0665   It is interesting that the shear-band spacing also plays a role in deformation of metallic glasses. Conner et al. [160] measured the spacing in quasi-static bending of a Zr-based BMG and found it to be ~ 0.1 mm initially. Eventually, a few shear bands grow and dominate the process as in the case of dynamic deformation, discussed in Section 3.11.

s0125 ## 3.14   Summary

p0670 In this chapter, we presented the results of individual and collaborative investigations on the microstructural aspects of shear localization in materials under high strain and high-strain rates with emphasis on our contributions. We also reviewed and discussed some important phenomena such as the evolution process of shear localization; the experimental criterion for shear-band formation; possible mechanisms for the generation of the deformed and transformed bands; dynamic/static recrystallization occurrence; phase transformation and transition of the crystalline lattice to amorphous phase; super high-strain-rate deformation and microstructures within the band; and shear localization in ultrafine-grained and nanostructured metals as well as metallic glasses.

p0675   Extreme deformation under high strain and high-strain rate is unique, enormously complex and beyond the realm of technology that utilizes common

stress–strain diagrams. Deformation at rates involving explosions, penetrate shatter, fragmentation and so on are also impossible to monitor and require innovative approaches to interpret the phenomenon and behaviour of matter in a period of several millionths of a second. A number of scientific questions still remain open, and further investigations and measurements are needed.

AU : 26

p0680   Advanced sample preparation and characterization tools as well as diagnostics are significantly accelerating our understanding of the nature of phenomenon. The focused ion beam (FIB), TEM, HREM and GESEM–EBSD techniques will play an important role in this endeavour.

AU : 27

u0080 • Real-time experimental examination of the 2D deformation in a propagating shear band has two components:

u0085   • Propagation velocity as a function of applied stress. The experiments developed by Zhou et al. [70] reveal an extremely important characteristic of shear bands: their propagation velocity. More systematic experimentation is needed to understand how the velocity is related to the constitutive response in metals and alloys. Is it possible to develop a generalized theory? Is the Mercier–Molinari [124] theory applicable over a broad spectrum?

u0090   • The temperature rise plays a key role in the formation of the shear bands but has not been determined precisely at present.

u0095 • Thermal softening at high rates. The microstructural changes that are well documented undoubtedly affect the thermal softening. However, the exact nature of this softening is virtually unknown. The thickness and spacing of bands are directly dependent on this softening. The constitutive approach by Molinari and Ravichandran [161] might be a good effect in that direction.

u0100 • A better understanding of the rate sensitivity of work hardening is needed for improved constitutive description. The Los Alamos MTS model pioneered by Kocks and co-workers [162] incorporates this effect through a dislocation evolution term, but the physical basis needs experimental verification.

u0105 • Concerning the ultrafine-grain size within the shear bands, what are the contributions of rotational recrystallization, post-deformation recrystallization and grain growth processes on the recovered microstructure?

u0110 • The self-organization of the bands is a new topic of study requiring both experimental and theoretical investigations. Further experimental investigation is needed to provide the modelling of such complicated behaviour.

u0115 • Both shear-band bifurcation and the development of a quantitative treatment of a shear-band toughness (initially proposed by Grady [141,142]) are desirable and necessary areas of research.

p0725   Finally, although there is rather good relation between theoretical analysis and experimental results, the experimental data that can be directly compared with these analyses to verify and guide model development of shear localization are still scarce. Material researchers need to provide clear descriptions of the nano/micro/mesostructural evolution, thus enabling mechanics performing theoretical analyses to arrive at more complete constitutive descriptions. Mechanics and material researchers should come together more often to accelerate the understanding of the phenomena.

s0130 ## Acknowledgements

References

1. Zener, C. and Hollomon, J.H. (1944). Effect of strain rate upon plastic flow of steel. J. Appl. Phys. 15, 22−32.
2. Recht, R.F. (1964). Catastrophic thermoplastic shear. J. Appl. Mech. 31, 189−193.
3. Culver, R.F. (1973). Thermal instability strain in dynamic plastic deformation. In Metallurgical Effect at High Strain Rates (R.W. Rohde, B.M. Butchern, J.R. Holland and C.H. Karnes eds.). Plenum Press, New York, NY, p. 519.
4. Bai, Y.L. (1981). A criterion for thermo-plastic shear instability. In Shock Waves and High-Strain-Rate Phenomena (L.E. Murr and M.A. Meyers eds.). Plenum Press, New York, NY, p. 277.
5. Burns, T.J. and Trucano, T.G. (1982). Instability in simple shear deformation of structural softening materials. Mech. Mater. 1, 313−326.
6. Pan, J. (1983). Perturbation analysis of shear strain shear in rate sensitive materials. Int. J. Solids Struct. 19, 153−164.
7. Semiatin, S.L., Staker, M.S. and Jonas, J.J. (1984). Plastic instability and flow localization in shear at high rates of deformation. Acta Mater. 32, 1347.
8. Wu, F.H. and Freund, L.B. (1984). Deformation trapping due to thermoplastic stability in one dimensional wave propagation. J. Mech. Phys. Solids 32, 119−132.
9. Freessengeas, C. and Molinari, A. (1987). Instability and localization of plastic flow in shear at high strain rates. J. Mech. Phys. Solids 35, 185−211.
10. Drew, D.A. and Flaherty, J.E. (1984). In Phase Transformation and Material AU : 29 Instabilities in Solids (M.E. Gurtin ed.). Academic Press, Orlando, FL, p. 37.

11. Tvergaard, V.J. (1987). J. Mech. Phys. Solids 35, 43.   AU : 30

12. Anderson, M.A., Fleck, N. and Johnson, K.L.J. (1990). J. Mech. Phys. Solids 38, 681.

13. Lemonds, J. and Needleman, A. (1986). Finite element analysis of shear localization in rate and temperature dependent solids. Mech. Mater. 5, 339−361.

14. Rogers, H.C. (1979). Adiabatic plastic deformation. Annu. Rev. Mater. Sci. 9, 283−311.

15. Timothy, S.P. (1987). The structure of adiabatic shear bands in metals: a critical review. Acta Mater. 35, 301−306.

16. Murr, L.E. and Pizana, C. (2007). Dynamic recrystallization: the dynamic deformation regime. Metall. Mater. Trans. 38A, 2611−2628.

17. Dormeval, R. (1987). The adiabatic shear phenomenon. In Materials at High Strain Rates (T.Z. Blazynski ed.). Elsevier, pp. 47−67.   AU : 31

18. Meyers, M.A. (2001). Encyclopedia of Materials: Science and Technology. Elsevier, pp. 7093−7103.

19. Malley, S.M. (2007). Shear localization: a historical overview. Metall. Mater. Trans. 38A, 2629−2654.

20. Xu, Y.B., Zhang, J.H., Bai, Y.L. and Meyers, M.A. (2008). Shear localization in dynamic deformation: microstructural evolution. Metall. Mater. Trans. 39A, 811−843.

21. Marchand, A. and Duffy, J. (1988). An experimental study of the formation process of adiabatic shear bands in a structural steel. J. Mech. Phys. Solids 36, 251−283.

22. Me-Bar, Y. and Shechtman, D. (1983). On the adiabatic shear of Ti−6Al−4V ballistic targets. Mater. Sci. Eng. 58, 181−188.

23. Timothy, S.P. and Hutchings, I.M. (1985). Initiation and growth of microfractures along adiabatic shear bands in Ti−6Al−4V. Mater. Sci. Technol. 1, 526−530.

24. Hartley, K.A., Duffy, J. and Hawley, A.H. (1987). Measurement of the temperature profile during shear band formation in steels deforming at high strain rates. J. Mech. Phys. Solids. 35, 283−301.

25. Bai, Y.L., Xue, Q., Xu, Y.B. and Shen, L.T. (1994). Characteristics and microstructure in the evolution of shear localization in Ti−6Al−4V alloy. Mech. Mater. 17, 155−164.

26. Xu, Y.B., Bai, Y.L. and Shen, L.T. (1996). Formation, microstructure and development of the localized shear deformation in low-carbon steels. Acta Mater. 44, 1917−1926.

27. Derep, J.L. (1987). Microstructure transformation induced by adiabatic shearing in armor steel. Acta Mater. 35, 1245−1249.

28. Giovanola, J.H. (1988). Adiabatic shear banding under pure shear loading, Part II: Fractographic and metallographic observations. Mech. Mater. 7, 73−87.

29. Cho, K., Chi, Y.C. and Duffy, J. (1990). Microscopic observation of adiabatic shear bands in three different steels. Metall. Mater. Trans. 21A, 1161−1175.

30. Liao, S.C. and Duffy, J. (1998). Adiabatic shear bands in a Ti−6Al−4V titanium alloy. J. Mech. Phys. Solids 46, 2201−2231.

31. Xue, Q., Meyers, M.A. and Nesterenko, N.F. (2002). Self-organization of shear bands in titanium and Ti−6Al−4V alloy. Acta Mater. 50, 575−596.

32. Meyers, M.A., Xu, M.A., Xue, Q., Perez-Prado, M.T. and McNelley, T.R. (2003). Acta Mater. 51, 1307−1325.   AU : 32

33. Batra, R.C. and Zhang, G.M. (2008). Modified smoothed particle hydrodynamics (MSPH) basis functions for meshless methods, and their application to axisymmetric Taylor impact test. J. Comput. Phys. 227, 1962−1981.

34. Xu, Y.B., Wang, Z.G., Huang, X.L., Shen, L.T. and Bai, Y.L. (1989). Microstructure of shear localization in low carbon ferrite-pearlite steel. Mater. Sci. Eng. A114, 81−87.

35. Meyers, M.A., Armstrong, R.W. and Kirchner, H. (eds.). (1999). Mechanics and Materials: Fundamentals and Linkages, John Wiley & Sons, pp. 1−15 (Chapter 1).   AU : 33

36. Guo, K.H. (1978). Electron Optical Microanalysis. Scientific Press, China, pp. 1−89.

37. Humphreys, F.J. (2001). Characterization of fine-scale microstructures by electron backscatter diffraction (EBSD). J. Mater. Sci. 36, 3833−3854.

38. Molinari, A. and Clifton, R.J. (1983). C. R. Acad. Sci. 296, 1.   AU : 34

39. Grady, D.E. and Kipp, M.E. (1987). J. Mech. Phys. Solids 35, 95.

40. Kuriyama, S. and Meyers, M.A. (1986). Metall. Mater. Trans. 17A, 443.

41. Wright, T.W. and Ockendon, H. (1996). Int. J. Plast. 12, 927.

42. Molinari, A. (1997). J. Mech. Phys. Solids 45, 1551.

43. Clifton, R.J., Duffy, J., Hartley, K.A. and Ghawki, T.G. (1984). Scr. Mater. 18, 44.

44. Bai, Y.L., Cheng, C. and Yu, S.B. (1986). Acta Mech. Sin. 2, 1.

45. Shawki, T.G. and Clifton, R.J. (1989). Shear band formation in thermal viscoplastic materials. Mech. Mater. 8, 13−43.

46. Liao, S.C. and Duffy, J. (1998). Adiabatic shear bands in a Ti−6Al−4V titanium alloy. J. Mech. Phys. Solids 46, 2201−2231.

47. Backman, M.E., Finnegan, S.A., Shulz, J.C. and Pringle, J.K. (1986). In Metallurgical Applications of Shock-Wave and High Strain-Rate Phenomena   AU : 35 (L.E. Murr, K.P. Staudhammer and M.A. Meyers eds.). Marcel Dekker, New York and Basel, p. 675.

48. Bai, Y.L. (1989). Evolution of thermo-visco-plastic shearing. In Proceedings of Materials at High Rates of Strain (J. Harding ed.). JOP Publishing, Bristol, p. 99.   AU : 36

49. Dodd, B. and Bai, Y.L. (1987). Ductile Fracture and Ductility with Application to Metalworking. Academic Press, London.

50. Costin, L.F., Crisman, E.E., Hartley, R.H., and Duffy, J. (1979). In Proceedings of the 2nd Conference on Mechanical Properties at High Rates of Strain (J. Harding ed.). Institute of Physics, Briston and London, p. 90.

51. Hartley, K.A., Duffy, J. and Hawley, R.H. (1987). Measurement of the temperature profile during shear band formation in steels deformation at high strain rates. J. Mech. Phys. Solids 35, 283−301.

52. Giovanola, J.H. (1988). Adiabatic shear banding under pure shear loading. Part I: Direct observation of shear localization and energy dissipation measurements. Mech. Mater. 7, 59−71.

53. Guduru, P.R., Rosakis, A.J. and Ravichandran, G. (2001). Dynamic shear band: an investigation using high speed optical and inferred diagnostics. Mech. Mater. 33, 371−402.

54. Xue, Q., Shen, L.T. and Bai, Y.L. (1995). A modified split Hopkinson torsional bar in studying shear localization. Meas. Sci. Technol. 6, 1557−1566.

55. Xue, Q., Shen, L.T. and Bai, Y.L. (1955). Elimination of loading reverberation in the split Hopkinson torsional bar. Rev. Sci. Instrum. 66, 5298−5304.

56. Xu, Y.B., Zhong, W.L., Chen, Y.J., Shen, L.T., Liu, Q., Bai, Y.L. and Meyers, M.A. (2001). Shear localization and recrystallization in dynamic deformation of 8090 Al−Li alloy. Mater. Sci. Eng. 299A, 287−295.

57. Timothy, S.P. and Hutchings, J.M. (1984). In Proceedings of 3rd International Conference on Mechanical Properties at High Rates of Strain (J. Harding ed.). Institute of Physics, Bristol, p. 397.

58. Molinari, A. (1988). In Nonlinear Phenomena in Material Science Solid State   AU : 37 Phenomena (G. Martin and L.P. Kubin eds.). Trans Tech Publications, Aedermannsdor, Switzerland, Vols. 3−4, pp. 447−468.

59. Wright, T.W. (2002). The Physics and Mathematics of Shear Bands. Cambridge   AU : 38 University Press.

60. Staker, M.R. (1981). The relation between adiabatic shear instability strain and material properties. Acta Mater. 29, 683−689.

61. Zurek, A.K. (1994). The study of adiabatic shear band instability in a pearlite 4340 steel using a dynamic punch test. Metall. Mater. Trans. 25A, 2483−2489.

62. Bai, Y.L. (1982). Thermo-plastic instability in simple shear. J. Mech. Phys. Solids 30, 195−207.

63. Xu, Y.B., Yu, J.Q., Shen, L.T. and Bai, Y.L. (2000). The thermoplastic shear localization in titanium alloys during dynamic deformation. Mater. Sci. Technol. 16, 609−611.

64. Me-Bar, Y. and Shechtman, D. (1983). Mater. Sci. Eng. 58, 181−188.   AU : 39

65. Grebe, A., Pak, H.-R. and Meyers, M.A. (1985). Adiabatic shear localization in titanium Ti6Al4V alloy. Metall. Mater. Trans. 16, 761−775.

66. Li, Q., Xu, Y.B. and Bassim, M.N. (2004). Dynamic mechanical behavior of pure titanium. J. Mater. Process. Technol. 155, 1889.

67. Welsh, N.C. (1957). J. Appl. Phys. 28, 960.   AU : 40

68. Cho, K., Chi, Y.C. and Duffy, J. (1990). Microscopic observation of adiabatic shear bands in three different steels. Metall. Mater. Trans. 21A, 1161−1174.

69. Meyers, M.A. and Wittman, C.L. (1990). Effect of metallurgical parameters on shear band formation in low carbon (approximately 0.20 wet. pct) steel. Metall. Mater. Trans. 21A, 3153−3164.

70. Zhou, M., Rosakis, A.J. and Ravichandran, G.J. (1996). Mech. Phys. Solids 44, 981.

71. Xu, Y.B. and Meyers, M.A. (2003). Microstructural evolution of localized shear bands induced during explosion in Ti−6Al−4V alloy. J. Mater. Sci. Technol. 19, 385−387.

72. Zou, L., Zhen, L., Xu, C.Y. and Shao, W.Z. (2011). Characterization of adiabatic shear bands in AM60B magnesium alloy under ballistic impact. Mater. Charact. 62, 496−502.

73. Trent, E.M. (1941). The formation and properties of materials on the surface of rope wire. J. Iron Steel Inst. 143, 401−419.

74. Scott, D., Loy, B. and Mills, G.H. (1967−1968). Inst. Mech. Eng. Proc. 181, 30.   AU : 41

75. Beatty, J.H., Meyer, L.W., Meyers, M.A. and Nemat-Nasser, S. (1992). Shock-Wave and High-Strain-Rate Phenomena in Materials. Marcel Dekker, New York, NY, pp. 645−656.

76. Duan, C.Z. (2004). Doctoral Thesis. Study on Microscopic Mechanism of Adiabatic Shear Behavior in Orthogonal Cutting of High Strength Steel. Dalian University of Technology.

77. Xu, Y.B., Yang, H.J. and Meyers, M.A. (2007). Dynamic recrystallization in the shear bands of Fe−Cr−Ni monocrystal: electron backscatter diffraction characterization. Scr. Mater. 58, 691−694.

78. Yang, H.J., Xu, Y.B., Seki, Y., Nesterenko, V.F. and Meyers, M.A. (2009). J. Mater.   AU : 42
Res. 24, 2617−2627.

79. Yang, H.J., Zhang, J.H., Xu, Y.B. and Meyers, M.A. (2008). Microstructural characterization of the shear bands in Fe−Cr−Ni single crystal by EBSD. J. Mater. Sci. Technol. 24, 819−828.

80. Kad, B.K., Gebert, J.-M., Perez-Prado, M.T., Kassner, M.E. and Meyers, M.A. (2006). Ultra-grain-sized zirconium by dynamic deformation. Acta Mater. 54, 4111−4127.

81. Xu, Y.B., Bai, Y.L. and Meyers, M.A. (2006). Deformation, phase transformation and recrystallization in the shear bands induced by high-strain rate loading in titanium and its alloys. J. Mater. Sci. Technol. 22, 737−746.

82. Staudhammer, K.P., Frantz C.E., Hecker, S.S., and Murr L.E. (1981). Effect of strain   AU : 43
rate on deformation-induced martensite in 304 stainless steel. In Shock Waves and High-Strain-Rate Phenomena in Metals and Alloys. Addison Dekker, pp. 91−111.

83. Murr, L.E. and Ross, M.F. (1968). Philos. Mag. 18, 281−295.   AU : 44

84. Kestenbach, H.J. and Meyers, M.A. (1976). Metall. Trans. 7A, 1943.

85. Olson, G.B. and Cohen, M.A. (1972). Mechanism for the strain-induced nucleation of martensitic transformation. J. Less Common Met. 28, 107−118.

86. Meyers, M., Cao, B.Y., Nesterenko, V.F., Benson, D. and Xu, Y.B. (2004). Shear localization-martensitic transformation in Fe−Cr−Ni monocrystal. Metall. Trans. 35A, 2575−2586.

87. Wang, B.F. and Yang, Y. (2008). Microstructure evolution in adiabatic shear band in fine-grain-sized Ti−3Al−5Mo−4.5V alloy. Mater. Sci. Eng. A 473, 306−311.

88. Costin, L.S. and Duffy, J. (1979). The effect of loading rate and temperature on the initiation of fracture in a mild rate-sensitive steel. J. Eng. Mater. Technol. 101, 258−264.

89. Shawki, T.G. (1994). An energy criterion for the onset of shear localization in thermal viscoplastic materials. 1. Necessary and sufficient conditions. J. Appl. Mech. Trans. ASME 61, 530−537.

90. Xu, Y.B., Ling, Z., Wu, X. and Bai, Y.L. (2002). Evolution of thermoplastic shear localization and related microstructures in Al/SiCp composites under dynamic compression. J. Mater. Sci. Technol. 18, 504−508.

91. Lee, S., Cho, K.M., Kim, K.C. and Choi, W.B. (1993). Metall. Mater. Trans. 24A, 895.   AU : 45

92. Zhou, M. (1998). Int. J. Plast. 14, 733.

93. Shih, C.J., Nesterenko, V.N. and Meyers, M.A. (1998). High-strain rate deformation and comminution of SiC. J. Appl. Phys. 9, 4660−4671.

94. Xu, Y.B., and Meyers, M.A. (2011). Transition of crystalline lattice to the amorphous phase in the shear bands induced under high-strain rate of Fe−Cr−Ni single crystal. Unpublished work.

95. Li, N., Wang, Y.D., Peng, R.L., Sun, X., Liaw, P.K., Wu, G.L., Wang, L. and Cai, H. N. (2011). Localized amorphism after high-strain rate deformation in TWIP steel. Acta Mater. 59, 6369−6377.

96. Meyers, M.A. and Park, H.-K. (1986). Acta Mater. 34, 2493.   AU : 46

97. Lins, J.F.C., Sandim, H.R.Z., Kestenbach, H.-J. and Raabe, D. (2007). Mater. Sci. Eng. A457, 205.

98. Chichili, D.R., Ramesh, K.T. and Hempker, K.J. (1998). Acta Mater. 46, 1025.

99. Murr, L.E., Niou, C.S., Pappu, S., Rivas, J.M. and Quinones, S.A. (1995). Phys. Status Solidi 149, 253.

100. Hines, J.A., Vecchio, K.S. and Ahzi, S. (1998). Metall. Trans. 29A, 191.

101. Nesterenko, V.F., Meyers, M.A., LaSalvia, J.C., Bondar, M.P., Chen, Y.J. and Lukyanov, Y.L. (1997). Shear localization and recrystallization in high-strain, high-strain rate deformation of tantalum. Mater. Sci. Eng. A229, 23−41.

102. Meyers, M.A., Chen, Y.J., Marquis, F.D.S. and Kim, D.S. (1995). Metall. Mater.   AU : 47
Trans. 26A, 2493−2501.

103. Martinez, F., Murr, L.E., Ramirez, A., Lopea, M.I. and Gaytan, S.M. (2007). Mater. Sci. Eng. A454−455, 581.

104. Meyers, M.A., LaSalvia, J.C., Nesterenko, V.F., Chen, Y.J., and Kad, B.K. (1997). Recrystallization and related phenomena. In Proceedings of Rex'96 (J.I. McNelley, ed.), Monterey, CA, p. 279.

105. Li, J.C.M. (1995). TMS Annual Meeting. Unpublished results.

106. Murr, L.E. (2001). Interfacial Phenomena in Metals and Alloys. Addison-Wesley, London and Amsterdam, p. 1.

107. Meyers, M.A., Nesterenko, V.F., LaSalvia, J.C. and Xue, Q. (2001). Mater. Sci. Eng.   AU : 48
A317, 204.

108. Xue, Q., Bingert, J.F., Henrie, B.L. and Gray, III, G.T. (2007). EBSD characterization of dynamic shear band regions in pre-shocked and as-received 304 stainless steels. Mater. Sci. Eng. A473, 279−289.

109. Rath, B.B. and Hu, B.B. (1972). In Nature and Behavior of Grain Boundaries (H. Hu ed.). Plenum Press, New York, NY, p. 405. AU : 49

110. Humphreys, F.J. and Hatherly, M. (1995). Recrystallization and Related Annealing Phenomena. Pergamon Press, Oxford.

111. Li, Q., Xu, Y.B., Lai, Z.H., Shen, L.T. and Bai, Y.L. (2000). Dynamic recrystallization induced by plastic deformation at high strain rate in a Monel alloy. Mater. Sci. Eng A276, 250−256.

112. Li, Q. (1999). Dynamic Mechanical Behavior, Plastic Deformation Localization and Formation of Ultrafine Grain Structures in Metallic Materials. Post-Doctoral Report. Institute of Metal Research, Chinese Academy of Sciences, Shenyang, China.

113. Hirth, J.P. and Lothe, J. (1968). Theory of Dislocations. McGraw-Hill, New York, NY.

114. Dodd, B. and Bai, Y.L. (1989). Width of adiabatic shear band formed under combined stresses. Mater. Sci. Eng. 5, 557−559.

115. Xing, D., Bai, Y.L., Chen, C.M. and Huang, X.L. (1991). On post instability processes in adiabatic shear in rot rolled steel. J. Mech. Phys. Solids 39, 1017−1042.

116. Ashby, M.F and Verrall, R.A. (1973). Diffusion-accommodated flow and super plasticity. Acta Mater. 21, 149−163.

117. Murr, L.E., Trillo, E.A., Pappu, S. and Kennedy, C. (2002). Adiabatic shear bands and examples of their role in severe plastic deformation. J. Mater. Sci. 37, 3337−3360.

118. Chokshi, A.H. and Meyers, M.A. (1990). Scr. Mater. 24, 605. AU : 50

119. Murr, L.E. (1987). Metallurgical effect of shock and high-strain-rate loading. In Materials at High Strain Rates (T.E. Blazynski ed.). Elsevier, London and New York, pp. 1−46.

120. Lee, S., Cho, K.-M., Lee, C.S. and Choo, W.Y. (1993). Metall. Mater. Trans. 26A, 2217. AU : 51

121. Meyers, M.A., Andrade, U.R. and Chokshi, A.H. (1995). Mech. Mater. Trans. 26A, 2881.

122. Brandon, D.G. (1987). In Materials at High-Strain Rates (T.E. Blazynski ed.). Elsevier, New York, NY, p. 187. AU : 52

123. Xue, Q. and Gray, G.T. (2006). Development of adiabatic shear bands in annealed 316L stainless steel. Part I: Correlation between evolving microstructure and mechanical behavior. Metall. Mater. Trans. 37A, 2435−2446.

124. Mercier, S. and Molinari, A. (1998). J. Mech. Phys. Solids 46, 1463. AU : 53

125. Xue, Q., Meyers, M.A. and Nesterenko, N.F. (2004). Self organization of shear bands in stainless steel. Mater. Sci. Eng. A384, 35−46.

126. Cottrell, A.H. (1953). Dislocations and Plastic Flow in Crystals. Oxford. AU : 54

127. Cottrell, A.H. (1953). Philos. Mag. 44, 829. AU : 55

128. Portevin, A. and Le Chatelier, F.C.R. (1923). C. R. Acad. Sci. 176, 507.

129. Portevin, A. and Le Chatelier, F. (1924). Trans. Am. Soc. Steel Treat. 530, 457.

130. McGregor, C.W. and Fisher, J.C.J. (1945). Appl. Mech. 12, A−217.

131. Baird, J.D. (1963). Iron Steel 36, 186, 326, 368, 400, 450

132. Morris, J.G. (1974). Mater. Sci. Eng. 13, 101.

133. Mulford, R.A. and Kocks, U.F. (1979). Acta Metall. 27, 1125.

134. Kocks, U.F., Cook, R.E. and Mulford, R.A. (1985). Acta Metall. 33, 623.

135. Nemat-Nasser, S., Guo, S. and Cheng, J.Y. (1999). Acta Mater. 47, 3705.

136. Bergstrom, Y. and Roberts, W. (1971). Acta Metall. 19, 815.

137. Li, C.C. and Leslie, W.C. (1978). Effects of dynamic strain aging on the subsequent mechanical properties of carbon steels. Metall. Trans. 9, 1765−1775.
138. Gilat, A. and Wu, X. (1997). Int. J. Plast. 13, 611.   AU : 56
139. Mishra, A., Martin, M., Thadhani, N.N., Kad, B.K., Kenik, E.A. and Meyers, M.A. (2008). High-strain-rate response of ultra-fine-grained copper. Acta Mater. 56, 2770−2783.
140. Xu, Y.B., Yang, H.J., and Meyers, M.A. (2011). Dynamic/Static Recrystallization in Forced Shear Bands of Ultra-Fine Grained Copper Under High-Strain Rate Loading. Unpublished work.
141. Grady, D.E. (1994). Mech. Mater. 17, 289.   AU : 57
142. Grady, D.E. (2007). TMS Symposium on Dynamic Behavior of Materials. TMS, Warrendale, PA.
143. Andrade, U.R., Meyers, M.A., Vecchio, K.S. and Chokshi, A.H. (1994). Acta Metall   AU : 58
     Mater. 42, 3183.
144. Li, Y.S., Tao, N.R. and Lu, K. (2008). Microstructural evolution and nanostructure formation in copper during dynamic plastic deformation at cryogenic temperatures. Acta Mater. 56, 230−241.
145. Hong, C.S., Tao, N.R., Huang, X. and Lu, K. (2010). Nucleation and thickening at shear band in nano-scale twin/matrix lamellae of a Cu−Al alloy processed by dynamic plastic deformation. Acta Mater. 58, 3103−3116.
146. Peker, A. and Johnson, W.L. (1993). A highly processable metallic glass $Zr_{41.2}Ti_{13.8}Cu_{12.5}Ni_{10.0}Be_{22.5}$. Appl. Phys. Lett. 63, 2342−2344.
147. Johnson, W.L. (1999). MRS Bull. 24(10), 42.   AU : 59
148. Inoue, A. (2000). Acta Mater. 48, 279.
149. Lewandowski, J.J. and Greer, A.L. (2006). Nat. Mater. 51, 3495.
150. Spaepen, F. (1997). Acta Mater. 25, 407.
151. Dai, L.H., Liu, L.F. and Bai, Y.L. (2002). Formation of adiabatic shear band in metal matrix composites. Int. J. Solid Struct. 41, 5979−5993.
152. Liu, L.F., Dai, H. and Bai, Y.L. (2005). J. Non Cryst. Solids 351, 3259.   AU : 60
153. Dai, L.H., Yan, M., Liu, L.F. and Bai, Y.L. (2005). Appl. Phys. Lett. 87, 14196.
154. Wright, W.J., Saha, R. and Nix, W.D. (2001). Localized heating during serrated plastic flow in bulk metallic glasses. Mater. Trans. 42, 642−649.
155. Wright, W.J., Schwarz, R.B. and Nix, W.D. (2001). Deformation mechanisms of the Zr40Ti14Ni10Cu12Be24 bulk metallic glass. Mater. Sci. Eng. A 319, 229−232.
156. Qu, R.T., Eckert, J. and Zhang, Z.F. (2011). J. Appl. Phys. 109, 083544.   AU : 61
157. Zhang, Z.F., Eckert, J. and Schultz, L. (2003). Acta Mater. 51, 1167.
158. Zhang, Z.F., He, G., Eckert, J. and Schultz, L. (2003). Phys. Rev. Lett. 91, 045505.
159. Jiang, W.H. and Atzmon, M. (2003). Acta Mater. 51, 4095−4105.
160. Conner, R.D., Li, Y., Nix, W.D. and Johnson, W.L. (2004). Acta Mater. 52, 2429.
161. Molinari, A. and Ravichandran, G. (2005). Mech. Mater. 37, 737−752.
162. Kocks, U.F. and Mecking, H. (2003). Prog. Mater. Sci. 48, 171−273.
163. Li, Q., Xu, Y.B. and Bassim, M.N. (2003). Dynamic mechanical properties in relation to adiabatic shear band formation in titanium alloy-Ti17. Mater. Sci. Eng. 358, 128−133.

s0135 **Uncited references**   AU : 28

p0740 [163]

NON-PRINT ITEM

Abstract

We describe the principal characteristics that define the structure of adiabatic shear bands in metals at the nanostructural and microstructural scale. We comment on deformed and transformed bands, a classification that was created based on optical microscopy observations related to the appearance of the shear band. Modern analytical techniques, described in Section 3.2, have added a great deal to our capability to look into the nanostructure of shear bands. Thus, a band in the optical microscope which appears to be transformed consists actually of nanocrystalline grains that resulted from the breakup of the original microstructure and exhibit radically different etching characteristics. The formation of shear bands is dictated by the thermoplastic instability induced under high strain and high-strain rate, and the resulting structure is governed by three principal factors: (a) the temperature rise in conjunction with the kinetics and thermodynamics of phase transitions; (b) the shear strains and stresses that govern the generation of defects (primarily dislocations and twins, but also displacive phase transitions); and (c) the temperature decrease and kinetics and thermodynamics of phase transitions. The rotational recrystallization mechanism, proposed to be responsible for the creation of ultrafine-grained and nanocrystalline structures, is presented.

We present examples of amorphization in a shear band. The effect of dynamic strain aging as it affects the thermal softening and strain-rate sensitivity is discussed. Topics of considerable contemporary importance are the formation of shear bands in nanocrystalline, ultrafine-grained and glassy (especially, bulk metallic glasses (BMGs)) materials. These materials are characterized by low work hardening and are prone to shear localization, even when the external rate of load application is low. In metallic glasses, the softening has been attributed to two sources: free volume effects and thermal effects. They are briefly discussed.

AU : 3